RAS Techniques and Instruments

RASTI **5,** 1–28 (2026)
Advance Access publication 2026 March 20

https://doi.org/10.1093/rasti/rzag022

High-precision photometry with a scientific CMOS camera: II on-sky testing of the Marana camera at the NGTS facility

Ioannis Apergis [1,2,3★] Daniel Bayliss [1,2] Paul Chote [1,3] James McCormac [1,2,3] Peter J. Wheatley [1,2] Morgan A. Mitchell [1,2] Jorge Fernández Fernández [1,2] Sam Gill [1,2] Edward M. Bryant [1,2] Toby Rodel [4] Leonidas Asimakoulas [5] David R. Anderson [6] James A. Blake [1,2,3] Sarah L. Casewell [7] Fintan Eeles-Nolle [1,2] Faith Hawthorn [1,2] James S. Jenkins [8,9] Monika Lendl [10] Isobel S. Lockley [1,2] Maximiliano Moyano,[6] Sean M. O'Brien [4] Suman Saha [8,9] Alexis M. S. Smith [11] Philip G. Steen,[5] Jose I. Vines,[6] Richard G. West [1,2] and Tafadzwa Zivave [1,2]

[1]*Department of Physics, University of Warwick, Gibbet Hill Road, Coventry CV4 7AL, UK*
[2]*Centre for Exoplanets and Habitability, University of Warwick, Gibbet Hill Road, Coventry CV4 7AL, UK*
[3]*Centre for Space Domain Awareness, University of Warwick, Gibbet Hill Road, Coventry CV4 7AL, UK*
[4]*Astrophysics Research Centre, School of Mathematics and Physics, Queen's University Belfast, Belfast BT7 1NN, UK*
[5]*Andor Technology Ltd, Springvale Business Park, 7 Millennium Way, Belfast BT12 7AL, UK*
[6]*Instituto de Astronomía, Universidad Católica del Norte, Angamos 0610, 1270709 Antofagasta, Chile*
[7]*School of Physics and Astronomy, University of Leicester, University Road, Leicester LE1 7RH, UK*
[8]*Instituto de Estudios Astrofísicos, Facultad de Ingeniería y Ciencias, Universidad Diego Portales, Av. Ejército Libertador 441, Santiago, Chile*
[9]*Centro de Excelencia en Astrofísica y Tecnologías Afines (CATA), Camino El Observatorio 1515, Las Condes, Santiago, Chile*
[10]*Observatoire de Genève, Université de Genève, Chemin Pegasi, 51, CH-1290 Versoix, Switzerland*
[11]*Institute of Space Research, German Aerospace Center (DLR), Rutherfordstr. 2, D-12489 Berlin, Germany*

Accepted 2026 March 16. Received 2026 February 23; in original form 2025 December 5

ABSTRACT

Modern scientific CMOS cameras offer very fast readout speeds and low read noise. In this study, we evaluate the performance of the Andor Marana CMOS camera through on-sky testing carried out at the NGTS facility at the ESO Paranal Observatory in Chile. We mount the Marana camera to an NGTS telescope, and conduct photometric observations of bright stars. In particular, we target transit events around eight known bright exoplanet host stars. Simultaneous observations are carried out using an existing Andor iKon-L CCD camera on a neighbouring NGTS telescope. This allows for a direct comparison of the photometric precision between the CMOS and CCD cameras. We find that the Marana CMOS exhibits a similar level of photometric performance to the CCD camera, achieving 500 ppm at a 30-min time-scale for a $T = 10$ mag star. Although the CCD has a slightly better quantum efficiency over the NGTS filter range (520–890 nm), we find that the faster readout speed of the CMOS compared to the CCD means that the CMOS camera detects 20 per cent more photons per unit time for a solar-type star in our standard 10 s exposure time operation mode. This results in the CMOS performing slightly better photometry in the photon-limited regime. We conclude that modern CMOS cameras, such as the Marana, are very well-suited for astronomical time-series photometry applications.

Key words: Instrumentation – Detectors – Sensors – CMOS – CCD – Exoplanets.

1 INTRODUCTION

Charge Coupled Device (CCD) cameras are an essential tool in modern astronomy, being at the heart of almost all astronomical instruments operating at optical wavelengths (C. D. Mackay 1986).

The major space-based exoplanet transit detection missions, such as *Kepler* (W. J. Borucki et al. 2010) and the Transiting Exoplanet Survey Satellite (*TESS*; G. R. Ricker et al. 2015) have been equipped with CCD detectors. The upcoming PLATO mission (H. Rauer et al. 2025) will also use CCD detectors. Similarly, ground-based transiting exoplanet surveys such as the Wide Angle Search for Planets (WASP; D. L. Pollacco et al. 2006) and its successor, the Next Generation Transit Survey (NGTS; P. J. Wheatley et al. 2018) have used CCD detectors. However rapid progress in Complementary Metal-Oxide Semiconductor (CMOS) technology, particularly over the past 10 yr such as low read noise and extended dynamic range mean that CMOS detectors may now be considered for future transiting exoplanet surveys (J. Ge et al. 2022).

★ E-mail: Ioannis.Apergis@warwick.ac.uk

© The Author(s) 2026.
Published by Oxford University Press on behalf of Royal Astronomical Society. This is an Open Access article distributed under the terms of the Creative Commons Attribution License (https://creativecommons.org/licenses/by/4.0/), which permits unrestricted reuse, distribution, and reproduction in any medium, provided the original work is properly cited.

Downloaded from academic.oup.com/rasti/article/doi/10.1093/rasti/rzag022/8530553 by claudia Legler user on 03 November 2026

CMOS cameras provide substantial advantages for dynamic celestial observations requiring rapid data capture and low read noise, such as detecting exoplanet transits (P. J. Wheatley et al. 2018), tracking asteroids (M. R. Alarcon et al. 2023), monitoring meteoroids (F. Kajino et al. 2019), detecting trans-Neptunian objects (S.-Y. Wang et al. 2024), and conducting space situational awareness observations to track and characterize satellites in near-Earth orbit (P. Zimmer, J. McGraw & M. Ackermann 2016; B. F. Cooke et al. 2023; J. A. Blake et al. 2023; P. Chote et al. 2025; R. J. S. Airey et al. 2025). Recent tests and observational campaigns have demonstrated the capability of CMOS sensors to produce high-quality photometry across a range of applications (M. R. Alarcon et al. 2023; H.-Y. Mu et al. 2024). CMOS cameras can achieve photometric precision comparable to that of CCDs, with accuracies reaching the millimagnitude level (K. Xiao et al. 2025). On-sky and detector noise sources measurements have been found to be in agreement with the theoretical noise models (C. Layden et al. 2025). In particular, modern back-illuminated CMOS detectors do not suffer the strong sub-pixel sensitivity variations associated with front-illuminated detectors (electrode structures, micro-lenses etc). (S. Karpov et al. 2020).

In this work, we set out to assess the performance of a CMOS camera in this context by deploying one at the NGTS facility, which is situated at a site with exceptional photometric qualities. We utilized a modern CMOS camera, the Marana 4.2BV-11, which has demonstrated great performance in laboratory tests (P. Qiu et al. 2021; S. Karpov et al. 2021; I. Apergis et al. 2025) and is expected to be well-suited for high-precision time-series photometry. By directly comparing the CMOS camera's performance with that of Andor's iKon-L CCD camera that is already installed on the NGTS telescopes, we test if CMOS technology can deliver comparable bright star photometry to the well-tested CCD cameras. This study provides valuable insight into whether CMOS image sensors could potentially compete with CCD image sensors in exoplanet surveys. By evaluating if CMOS devices exhibit similar noise characteristics and performance, we aim to determine their suitability as trusted instruments for precise, stable photometric measurements.

Our first paper (I. Apergis et al. 2025) evaluated the performance of the Marana CMOS camera under controlled laboratory conditions. We measured the camera's read noise in dark environments and characterized both the temporal and spatial noise patterns across sensor rows and columns. We examined the behaviour of the dark current and glow at different operating temperatures. Under illuminated conditions, we quantified the photon response non-uniformity and assessed the camera's linearity performance. Additionally, we measured the quantum efficiency of the sensor across multiple wavelengths and determined the transmittance of the front window mounted on the camera. Those results are summarized in Table 1. Overall, the performance of the Marana camera demonstrates that it is well suited for high-precision time-series photometry.

In this second paper, we focus on on-sky testing of the Marana CMOS, and making a direct comparison to the iKon-L CCD cameras. To do this, we take observations simultaneously with the CMOS and CCD cameras, with identical hardware configurations for the mount, telescope, filter, and with the same sky conditions. An identical pipeline is used to perform data reduction and photometry routines for both cameras.

This paper reports on on-sky tests of the Marana CMOS with the NGTS facility. It is organized as follows, in Section 2 we describe the NGTS facility and the CMOS and CCD cameras. In Section 3 we set out the methodology, including the installation of the CMOS camera at NGTS, the on-sky observations made with the CMOS and CCD cameras, and the image reduction and photometry pipeline. In Section 4 we discuss the various sources of photometric noise that are present in our CMOS and CCD data. In Section 5 we present our photometric results for the CMOS and CCD cameras from the on-sky testing. In Section 6 we discuss the results from the CMOS on-sky testing. Lastly, Section 7 outlines our conclusions on the suitability of the CMOS camera for bright star photometry.

Table 1. Specifications of the Marana CMOS camera (I. Apergis et al. 2025) in comparison with the iKon-L 936 CCD (P. J. Wheatley et al. 2018).

Camera	CMOS	CCD
Model	Marana 4.2B-11	iKon-L 936
Digital output	HDR, 16-bit	16-bit
Readout modes	100 MHz	3MHz
Gain e^-/ADU	1.131	1.99
Full Well Capacity, $e^- pix^{-1}$	69 026	82000
Non-Linearity, per cent	0.122	1
Read Noise, $e^- pix^{-1}$	1.571	12.9
Dark Current, $e^- pix^{-1} sec^{-1}$	1.617@−25°C	0.005@−70°C
PRNU[a], per cent	0.131	1.79
DSNU[b], e^-	0.232	3.79
Readout time, s	0.042	1.5
Detector size, mm	22.5 × 22.5	27.6 × 27.6
Pixel size, μm	11	13.5
NGTS Pixel scale, arcsec pix^{-1}	4.01	5.01
NGTS Field of view, deg	2.27 × 2.27	2.84 × 2.84
Shutter	Shutterless	45 mm Mechanical
Weight, Kg	3.0	4.6

Note. [a] Photo response non-uniformity, [b]Dark signal non-uniformity.

2 OBSERVATORY AND INSTRUMENTS

2.1 The NGTS facility

The Next Generation Transit Survey (NGTS; P. J. Wheatley et al. 2018) is a ground-based observatory located at ESO's Paranal Observatory in Chile. Inspired by the success of the WASP programme (D. L. Pollacco et al. 2006), NGTS was built to provide very high precision time-series photometry for bright stars to detect and characterize transiting exoplanets.

NGTS is comprised of 12 Newtonian telescopes, each with $f/2.8$ and 20 cm apertures, manufactured by AstroSysteme Austria.[1] The telescopes are spaced 2 m apart, in two rows of six, in a single enclosure. The optical design of the telescopes include a primary hyperbolic mirror along with a corrector lens. The telescopes are equipped with deep-depleted CCD cameras with high sensitivity in the red spectrum (see Section 2.2). These CCD cameras are mounted on a customized focuser with an NGTS-specific filter, designed for the 520–890 nm range. The quantum efficiency of the cameras is shown in Fig. 1. Further details about the instruments and the operation can be found in P. J. Wheatley et al. (2018).

The NGTS facility has successfully discovered 36 exoplanets and 8 eclipsing binaries.[2] Notable discoveries include NGTS-1b (D. Bayliss et al. 2018), a rare giant planet around a low mass

[1] https://www.astrosysteme.com/references/observatory-paranal-chile/
[2] https://ngtransits.org/pages/tabs/publications_page.html

Downloaded from academic.oup.com/rasti/article/doi/10.1093/rasti/rzag022/8530553 by claudia Legler user on 03 November 2026

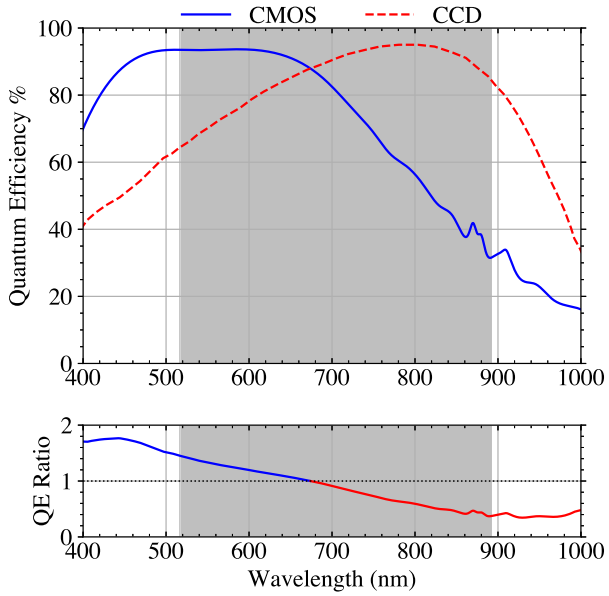


Figure 1. *Top:* QEs of the cameras as a function of wavelength. The filled grey area shows the NGTS custom filter. The blue line is the QE for the Marana CMOS camera and the red dashed line is the QE of the iKon-L CCD. *Bottom:* The ratio of the QE (CMOS/CCD).

star, NGTS-4b (R. G. West et al. 2019), the shallowest ever transit to be initially detected from a ground-based observatory, NGTS-10b (J. McCormac et al. 2020), a very short-period hot Jupiter, NGTS-14Ab (A. M. S. Smith et al. 2021), an exoplanet in the Neptunian desert and NGTS-30b (M. P. Battley et al. 2024), a very young long-period warm Jupiter. NGTS photometry has been shown to be scintillation limited (S. M. O'Brien et al. 2022) for bright stars $T < 12$ mag. The scintillation noise has been proven to be uncorrelated between the telescopes and therefore NGTS is capable of reaching the precision of *TESS* for stars of around $T = 9$ mag (E. M. Bryant et al. 2020) when combining data from multiple telescopes.

Currently NGTS is focused primarily on discovering long period transiting exoplanets based on *TESS* mono-transits or duo-transits (S. Gill et al. 2020a, c; S. Ulmer-Moll et al. 2022; F. Hawthorn et al. 2024). Additionally, NGTS observes targets from a range of science areas, including bright exoplanet host stars (D. Bayliss et al. 2020, 2022), targeted open cluster surveys (e.g. E. Gillen et al. 2020), long period eclipsing binaries (e.g. S. Gill et al. 2020b; T. Rodel et al. 2025), transiting brown dwarfs (e.g. B. A. Henderson et al. 2024), and stellar flares (e.g. J. A. G. Jackman et al. 2023).

2.2 The iKon-L 936 CCD camera

The iKon-L 936 BR-DD is a CCD camera[3] that was developed by Andor Technologies. It features a back-side deep depleted sensor with 2048 × 2048 pixels with pixel dimension 13.5 μm each. The sensor is made by e2v and it is enhanced with fringe suppression and dual anti-reflection coatings.

The iKon-L CCD serves as the primary camera for NGTS, mounted on all NGTS telescopes. It provides high sensitivity in the red wavelengths, achieving QE > 90 per cent at 750 nm (see Fig. 1), which is particularly advantageous for observing K and M dwarf stars. Equipped with a five-stage Peltier thermoelectric cooling system, the CCD maintains minimal dark current at operating temperatures as low as −100° C. Additionally, it features vacuum sealing, protecting it from environmental influences and enabling long-term operation without the need for replacement or servicing.

The camera underwent extensive laboratory testing (P. J. Wheatley et al. 2018) (see Table 1) before NGTS commissioning and successful deployment in 2015. NGTS operates the iKon-L CCD camera in the 3 MHz readout mode and at −70 ° C constant temperature. Typically NGTS uses 10 s exposure time for imaging followed by 1.5 s readout. However, additional delays are introduced due to autoguiding corrections and per-image statistical calculations. Furthermore, the mount requires a short settling period before the shutter can reopen. Altogether, these factors result in a total dead time between the images of approximately 3 s.

2.3 The Marana CMOS camera

The Marana 4.2B-11 Camera[4] is a CMOS device featuring a thinned, back-side illuminated sensor. The sensor has 2048 × 2048 pixels, with pixel dimension 11 μm. It offers low read noise, an extended dynamic range thanks to the high dynamic range (HDR) mode, and high sensitivity across the visible spectrum, with quantum efficiency peaking at 95 per cent at 550 nm (see Fig. 1). The sensor is housed within a vacuum chamber, which helps preserve sensor quality by effectively preventing condensation and dust accumulation. The five stage Peltier thermoelectric cooler enables operating temperatures down to −25 ° C air-cooled. The camera also provides fast readout speeds and high frame rates, enabling high-cadence monitoring. The performance of the Marana CMOS is summarized in Table 1.

For the on-sky testing at NGTS presented in this work, the CMOS camera was operated in HDR mode. This is the default mode for astronomical applications, offering low read noise and an extended dynamic range. The extended dynamic range and low read noise are achieved through the implementation of two pixel-level pre-amplifiers: a High Gain and a Low Gain. The signal from each pixel is processed simultaneously along both gain paths, with the High Gain channel optimized for low illumination levels and the Low Gain channel for high illumination levels. Each gain channel is digitized using a 12-bit analogue-to-digital converter (C. Ma & X. Wang 2013; X. Tang et al. 2020; S. Lou et al. 2023). At the start of an exposure, once the High Gain channel becomes saturated, the system switches to the Low Gain channel (see further discussion in Section 6.3). The final output frame is reconstructed by combining the two gain channels into a single 16-bit image, producing a HDR output (see I. Apergis et al. 2025, for details).

We operate the camera at a constant temperature of −25 ° C. Based on the temperature information recorded in the image headers, no significant fluctuations were observed, and the detector temperature remained stable at the set point throughout the observations. We set the exposure time to be 10 s in order to match that of the iKon-L CCD camera.

[3] https://andor.oxinst.com/products/ikon-xl-and-ikon-large-ccd-series/ikon-l-936

[4] https://andor.oxinst.com/products/scmos-camera-series/marana-scmos

Downloaded from academic.oup.com/rasti/article/doi/10.1093/rasti/rzag022/8530553 by claudia Legler user on 03 November 2026



Figure 2. The Marana sCMOS camera, highlighted within the blue rectangle, is mounted on one of the NGTS telescopes while capturing flat-field images during evening twilight at Cerro Paranal, Chile.

The Marana camera applies internal pre-processing corrections intended to improve image quality. These include Anti-glow correction, which mitigates glow artefacts visible in dark exposures, and the Spurious Noise Filter, which replaces noisy pixels by averaging neighbouring pixels (see I. Apergis et al. 2025, for details). For the analysis presented here, the Spurious Noise Filter was disabled, while the Anti-glow correction was enabled.

3 METHODS

3.1 Installation of the Marana CMOS camera at NGTS

In December 2023 we installed a Marana CMOS Camera on one of the NGTS telescopes (telescope ID 06). For this installation we removed the existing iKon-L CCD from the telescope and mounted the Marana CMOS using a custom camera faceplate to achieve the correct telescope back focus distance. As the Marana CMOS is 1.6 kg lighter than the iKon-L CCD camera, the telescope was rebalanced, which was achieved by removing some of its counterweights. Fig. 2 shows the Marana CMOS camera mounted on the NGTS telescope.

To operate the Marana CMOS camera on NGTS, we installed an Intel NUC 11 Extreme Kit Core control computer in a small cabinet next to the pier of the telescope. This control computer was equipped with an i9 CPU, 32 GB RAM and 4 TB SSD running the `Rocky 9` Linux operating system. The Marana CMOS camera was connected to the control computer via a USB 3.0 connection. This control computer allowed us to operate the Manara CMOS camera independently and without affecting the other eleven NGTS telescopes and cameras.

The control computer operated both telescope and camera using the Robotic Observatory Control kit (`Rockit`),[5] a software package designed for managing ground-based robotic observatories. `Rockit` is also used at the University of Warwick's facilities at the Roque de los Muchachos Observatory (e.g. R. J. S. Airey et al. 2025; M. A. Mitchell et al. 2026). It follows a modular architecture in which background daemons run continuously to handle specific tasks such as telescope control, focusing, instrument management, and overall observatory coordination. These daemons seamlessly interact with each other through a remote procedure call interface, enabling the execution of functions and procedures on remote programs. To facilitate this communication, `Rockit` uses the python library `Pyro4`.

Similarly to NGTS, to maintain the stability of the stars in the images and minimize systematic errors and noise from tracking inaccuracies, we use the `DONUTS` algorithm (J. McCormac et al. 2013). This innovative python package functions as an autoguiding algorithm, maintaining pixel drift at an accurate subpixel level relative to the first image, which serves as the reference frame. This approach meets our high precision photometry requirements and ensures consistent software performance between the CMOS and CCD cameras.

3.2 Observations

Observations were conducted from December 2023 to September 2024, during which time the CMOS camera was mounted on one of the NGTS telescopes. We also utilized one of the eleven available CCD cameras on a neighbouring telescope (telescope ID 01) for simultaneous observations. To maintain consistency and ensure photometric stability, the same CCD camera was used for comparison with the CMOS camera throughout the entire campaign. We made observations of well-known transiting exoplanets around bright stars, including WASP (D. L. Pollacco et al. 2006) and KELT (J. Pepper, A. Gould & D. L. Depoy 2004) host stars, as well as confirmed TOI systems. The targets are shown in Table 2. For the remainder of the time, the CMOS camera and telescope observed the same fields as the CCD on telescope ID 01, which were primarily *TESS* mono-transit and duo-transit candidates monitored as part of the NGTS program to discover long period exoplanet systems from *TESS* (F. Hawthorn et al. 2024; S. Gill et al. 2024).

The nightly schedule for the CCD on Telescope ID 01 was replicated and scheduled in the `Rockit` software to ensure the CMOS camera on Telescope ID 06 observed the exact same field centre as the CCD camera. This setup guaranteed that both cameras monitored the same area of sky simultaneously, although we note the CMOS camera has a smaller field-of-view (see Table 1). This strategy maintained consistency in observation duration and coverage between the CMOS and the CCD image sensors which we use for comparisons in this work. The CCD camera operated with an exposure time of 10 s and a cadence of 13 s. For consistency, the CMOS camera was configured with a 10 s exposure time and a total cadence of 10.042 s. NGTS uses a custom filter that covers a wavelength range of 520–890 nm (see Section 2 and Fig. 1). We used this same filter for the observations made using the CMOS camera, although we note the filter is not optimized for the bluer CMOS sensor's quantum efficiency (see Fig. 1). The images from the Marana CMOS camera were saved as FITS files onto the CMOS control computer. Instrument parameters were saved into the FITS file headers, including the JD timestamps, telescope coordinates, and camera settings.

In this paper we analyse data from nights where known transiting exoplanet systems were observed. We observed eight transiting exoplanets in total, with three of them observed twice. We also

[5] https://github.com/rockit-astro

Downloaded from academic.oup.com/rasti/article/doi/10.1093/rasti/rzag022/8530553 by claudia Legler user on 03 November 2026

Table 2. Simultaneous transit observations of bright stars with CMOS and CCD cameras.

Target	TIC ID	*TESS* Magnitude ∗	$T_{\rm eff}$ (K) ∗	Observation Date	Observation duration (h)	Transit fraction
TOI-905 (A. B. Davis et al. 2020)	TIC 261 867 566	10.57	5380 ± 130	2024-Jul−13	5.7	Full
WASP-95 (C. Hellier et al. 2014)	TIC 144 065 872	9.49	5760 ± 130	2024 Jul 14 & Aug 8	7.4 & 8.8	Full
TOI-2109 (I. Wong et al. 2021)	TIC 392 476 080	9.78	6650 ± 130	2024 Jul 17	5.5	Full
KELT-10 (R. B. Kuhn et al. 2016)	TIC 269 217 040	10.27	5890 ± 130	2024 Aug 01 & 26	8.3 & 6.5	Ingress
WASP-4 (D. M. Wilson et al. 2008)	TIC 402 026 209	11.82	5500 ± 140	2024 Aug 02	7.4	Full
WASP-97 (C. Hellier et al. 2014)	TIC 230 982 885	9.96	5700 ± 130	2024 Aug 04 & 6	5.6 & 5.7	Egress & Full
TOI-4463 (S. W. Yee et al. 2023)	TIC 8 599 009	10.46	5540 ± 140	2024 Aug 27	4.2	Full
WASP-30 (D. R. Anderson et al. 2011)	TIC 9 725 627	10.97	6360 ± 130	2024 Aug 28	7.9	Full

Note. ∗ source: TIC v8.2 (K. G. Stassun et al. 2018).

analyse two nights of observations taken on a dark night with no moon (2024 July 5) and a bright night with full moon (2024 June 22), both centred on the star TIC-188620407 (R.A.= $23^{\rm h}20^{\rm m}12\overset{\rm s}{.}37$, Dec= $-13^\circ5'56\overset{''}{.}83$, T = 11.57 mag).

3.3 Image reduction and photometry pipeline

For each observation, we execute a custom pipeline daily to extract photometry for each observed field. We solve each image astrometrically using the World Coordinate System (WCS), accounting for the field centre and pixel scale, with the help of *astrometry.net* (D. Lang et al. 2010). This software solves each image using a simple polynomial model. However, we identify weaknesses in the solution near the image corners, caused by distortions from the telescope's optics. To address this, we incorporate the *TESS* Input Catalogue version 8 (TIC8; K. G. Stassun et al. 2018) to identify sources in the field, particularly those brighter than $T < 16$ mag. Using the initial WCS solution, we iteratively refine the polynomial fit until we achieve sub-pixel accuracy (see P. Chote et al. 2025, for details). We exclude from the data set any images for which the WCS solution fails; these are typically outliers.

For the selections of stars for photometry, we used TIC8 (K. G. Stassun et al. 2018) with an upper cut of $T < 14$ mag. We apply criteria for blended stars, excluding stars that have a source identified within a 6 pixel radius (24 arcsec) around the star and a maximum magnitude difference of 2.5 magnitudes for a star to be considered as blended. Additionally, we exclude stars near the edges of the sensor. The same extracted catalogue for the CMOS image sensor is used for the CCD image sensor, since the FOV is larger due to the larger pixel scale, ensuring that both fields will contain the same stars.

We acquired dark and bias images when we were on-site, using the telescope cover to prevent external light from reaching the sensor. The properties and the long-term stability of the CMOS camera's bias and dark frames are discussed extensively by I. Apergis et al. (2025). We record evening and morning flat-field images before and after the science observations. We averaged the dark and bias frames to remove the electronic and thermal signal from each camera, and we create an averaged and normalized flat-field image for flat correction.

For the CCD camera, a flat-field correction was not applied, primarily because the autoguiding system keeps stellar positions stable to within sub-pixel deviations (<0.1 pixel RMS in X and Y positions over a typical observing night), ensuring that the same pixels are used consistently throughout the night (J. McCormac et al. 2013). The CMOS camera also exhibits sub-pixel positional stability. We performed photometry both with and without applying flat-field corrections for the CMOS data and found no noticeable difference. For a typical sample of stars, we find that omitting flat-field correction results in an RMS scatter improvement of approximately 0.29 per cent. Therefore, we adopted the same approach as for the CCD camera and did not apply a flat-field correction.

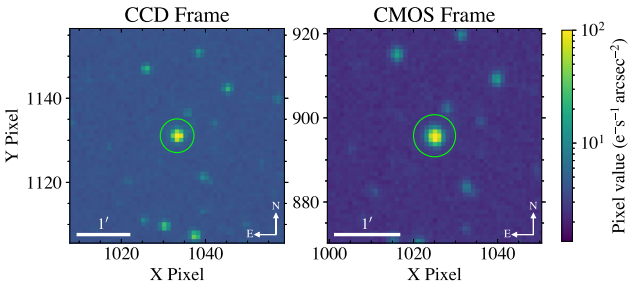


Figure 3. Target pixel frame (50 × 50 pixels) for CCD on the left and CMOS on the right. The selected photometric apertures for each camera are shown with green circles for target star KELT-10 (TIC-269217040, T = 10.27 mag) observed on 2024 August 1.

As part of the pipeline, we also verify that the autoguiding system is performing well by measuring the offsets between images using the `DONUTS` software (J. McCormac et al. 2013) to ensure that stars remain on the same pixels. We set an upper limit for the x-y positional shifts in the images; any frames exceeding this threshold – such as those affected by satellite trails or guiding lasers from the Very Large Telescope – are excluded from the data. In most cases, the autoguiding performed well within the specified pixel shift threshold.

To perform aperture photometry we extract the position for each star from the catalogue. We use the `SEP` python package (E. Bertin & S. Arnouts 1996; K. Barbary 2016) with circular apertures of specific radii defined for each camera as set out in Section 4. We define a sky background map from the `SEP` option to measure the sky background signal. An example of the target pixel frames for each camera is shown in Fig. 3.

We perform relative photometry to correct the light curves for atmospheric extinction, colour-dependent extinction, and any other systematics common to stars within the image. For each star, we collect its *Gaia* DR3 $G_{\rm BP} - G_{\rm RP}$, *TESS* magnitude, and TIC ID. We define magnitude and colour ranges for selecting comparison stars, with a bright magnitude limit of $T = 9.4$ mag, which usually indicates saturation in a 10 s image.

We establish criteria for the comparison stars by finding the best RMS value for each star within a particular magnitude range. Noisy stars are then excluded (see Section 5.3). The remaining

Downloaded from academic.oup.com/rasti/article/doi/10.1093/rasti/rzag022/8530553 by claudia Legler user on 03 November 2026

comparison stars are combined to produce a master reference star that corrects for the systematics affecting the target star.

4 PHOTOMETRIC NOISE

There are several sources of photometric noise that are well known and can be calculated for both the CMOS and CCD cameras. We construct the photometric noise model using the read noise and dark current of each camera (see Table 1), the sky background brightness and the target shot noise, and the expected scintillation noise at Paranal Observatory (S. M. O'Brien et al. 2022). In order to be able to compare the CMOS and CCD cameras, we express the photometric noise in terms of electrons using the conversion factor (gain) from analogue digital units to electrons (see Table 1). Since the pixel size is different between the CMOS (11 μm) and the CCD (13.5 μm) image sensors, we calculate the photometric noise for a photometric aperture of a fixed physical radius of almost exactly 55 μm, which equates to a radius of 5 pixels for the CMOS image sensor and 4 pixels for the CCD image sensor. The typical full-width half-maximum (FWHM) of the NGTS point-spread-function is 19 μm, therefore a photometric aperture of 55 μm was found to be optimal for our stars with magnitudes in the range $9 < T < 11$ (S. B. Howell 2000).

4.1 Detector noise

The two major sources of detector noise for digital imaging are read noise and dark current. Read noise is introduced during the process of the charge to voltage conversion and the conversion from analogue to digital values. Read noise includes all the noise sources which are independent of the exposure and the incoming signal (S. B. Howell 2000). Traditionally, CMOS image sensors have exhibited higher read noise compared to CCDs, primarily due to the complex circuitry, the large number of amplifiers, and their lower quality in earlier designs. However, advancements in CMOS image sensors such as the Marana camera have enabled the achievement of low read noise levels. The median read noise of the Marana camera was found to be 1.57 e^- (I. Apergis et al. 2025). Furthermore, while CCD image sensors struggle to maintain low read noise at high readout speeds, CMOS active pixel sensors are superior in this regard due to their unique amplifier-per-pixel design. For more details related to the read noise of the Marana CMOS camera see I. Apergis et al. (2025).

Dark current is thermal noise produced by the generation of heat within the sensor and it is dependent on the selected exposure time and temperature of the detector (e.g. W. Shockley & W. T. Read 1952; A. G. Aberle, S. W. Glunz & W. Warta 1992). Unlike the passive pixel design of CCDs, CMOS image sensors employ active pixels to amplify the signal on a per-pixel basis (K. D. Stefanov 2022). However, this additional circuitry can emit infrared photons from either the sensor periphery or the pixel amplifier transistor (J. Janesick et al. 2007; X. Wang et al. 2015). This glow effect is distinguishable from the dark current at low temperatures, since it exhibits a weaker temperature dependence than the dark current (see fig. 14 in I. Apergis et al. 2025, for details). Consequently, as the detector temperature decreases, the relative contribution of the glow component becomes more significant. The dark current for the Marana camera was measured to be 1.617 e^- pix^{-1} s^{-1} at constant temperature of $-25\,^\circ$C. For further details on dark current and glow in the Marana CMOS camera, refer to I. Apergis et al. (2025).

4.2 Sky background noise

Sky background is a major source of photometric noise in astronomy, especially when monitoring faint objects. Sky background signal consists of all the light entering the photometric aperture other than light from the target object. This may be from scattered light, background astrophysical sources, zodiacal light, and atmospheric effects such as moonlight or air-glow from night-sky emission lines (T. Maihara et al. 1993; S. Wüst et al. 2022). The mean sky background signal is subtracted from the photometric aperture during the photometric extraction (see Section 3.3). However, the sky background noise will contribute to the Poisson photon noise. The CMOS and CCD cameras show differing amounts of sky background noise largely due to the differences in the quantum efficiency of the cameras over the wavelength range of the NGTS filter (see Fig. 1).

4.3 Source noise

For ground-based photometric observations, the noise contribution due to light from the target star has two components – Poisson shot noise and scintillation noise. Poisson shot noise from the target star is simply given by the square root of the measured brightness of the star in electrons.

Scintillation noise arises from the fact that incident light from the target star will fluctuate in intensity as it moves through turbulent regions in the Earth's atmosphere (J. Osborn et al. 2015). This effect causes the star to 'twinkle'. Scintillation is particularly noticeable for small aperture telescopes observing bright stars (S. M. O'Brien et al. 2022), where it becomes a dominant source of noise. We calculate the expected scintillation noise for NGTS using a modified version of Young's formula (A. T. Young 1967; J. Osborn et al. 2015):

$$\sigma_{\rm sc}^2 = 10^{-5} C_{\rm Y}^2 D^{-4/3} t_{\rm exp}^{-1} \sec^3(z) \exp(-2h_{\rm o}/H), \quad (1)$$

where D is the diameter of the telescope (0.2 m for NGTS), $t_{\rm exp}$ is the exposure time (10 s for our observing), sec(z) denotes the airmass, $h_{\rm obs}$ is elevation above sea level (2433 m for NGTS), and H is the atmospheric scale height (we adopt 8000 m from J. Osborn et al. 2015). C_Y is an empirical coefficient that quantifies the amplitude of scintillation on a given night. We adopt the median value for Paranal Observatory of $C_Y = 1.54\,m^{2/3}s^{1/2}$ as reported by S. M. O'Brien et al. (2022).

Unlike the Poisson shot noise from the star, the fractional scintillation noise is *independent* of the flux from the target star (S. M. O'Brien et al. 2022). Thus for bright stars, scintillation noise will form a hard limit to the fractional photometric noise.

4.4 Total noise

The total photometric noise is the quadrature sum of the individual noise sources for a given photometric aperture, as the noise will be statistically independent (S. B. Howell 1989):

$$\sigma_{\rm total} = \sqrt{{\sigma_{\rm flux}}^2 + {\sigma_{\rm sky}}^2 + {\sigma_{\rm DC}}^2 + {\sigma_{\rm RN}}^2 + f^2{\sigma_{\rm sc}}^2}, \quad (2)$$

where $\sigma_{\rm flux}$ is the photon shot noise, $\sigma_{\rm sky}$ is the background signal noise, $\sigma_{\rm DC}$ is the dark current noise, $\sigma_{\rm RN}$ is the read noise, f is the flux from the target star, and $\sigma_{\rm sc}$ is the scintillation noise. In order to calculate the photometric noise expected for a star of a given magnitude, we must convert from flux in electrons (f) to

Downloaded from academic.oup.com/rasti/article/doi/10.1093/rasti/rzag022/8530553 by claudia Legler user on 03 November 2026

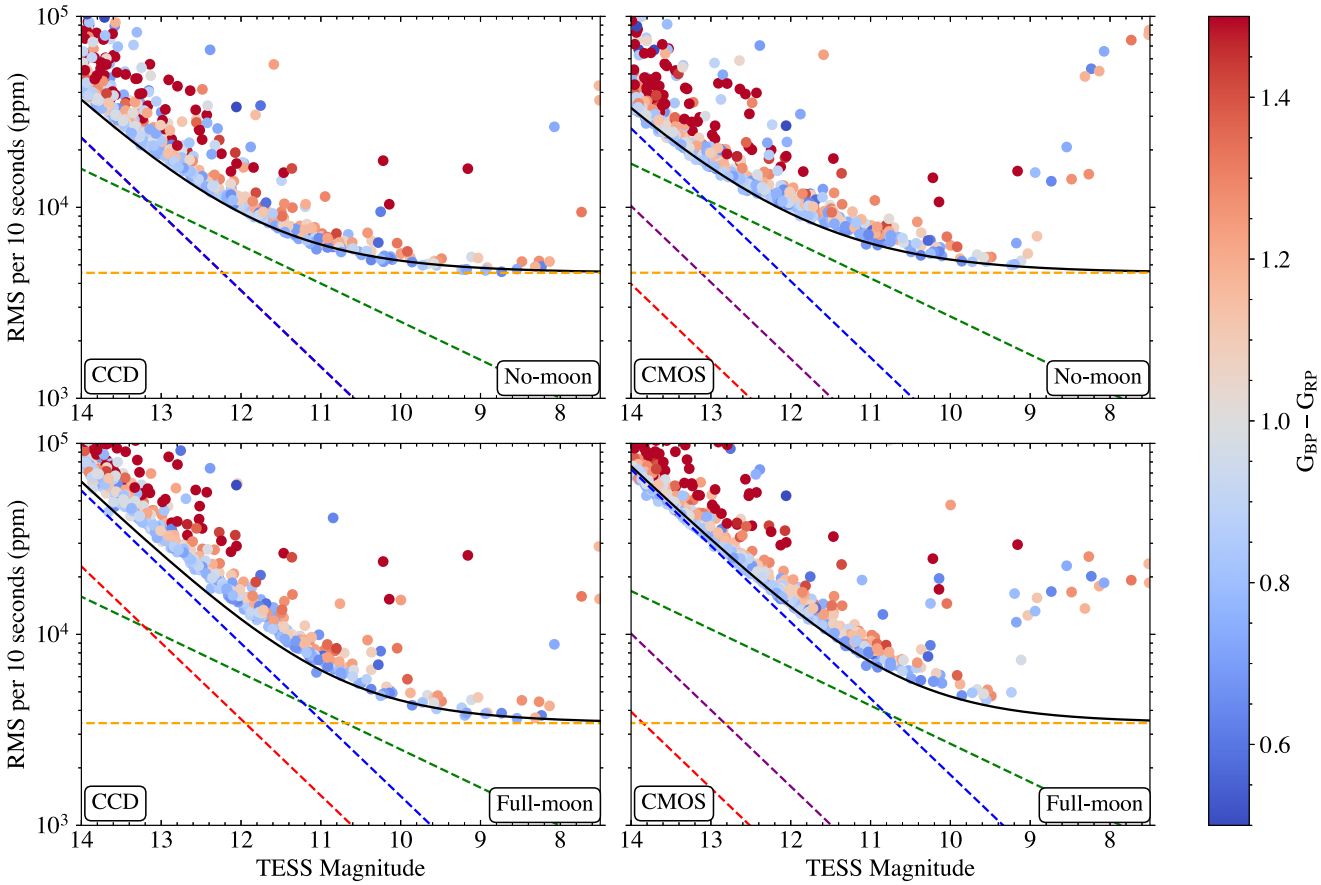


Figure 4. Photometric precision as a function of stellar magnitude for 10 s exposure predicted by the theoretical model and from observations during the new moon on 2024 July 5 (upper panels) and full moon on 2024 June 22 (lower panels). The left panels represent data from the CCD, while the right panels correspond to the CMOS. The dark line indicates the total modelled noise, including contributions from scintillation (yellow), photon shot noise (green), dark current noise (purple), sky background noise (blue), and read noise (red). The data points are coloured according to the *Gaia* DR3 $G_{BP} - G_{RP}$ colour and represent the measured noise in the detrended light curves from relative photometry of 746 stars with $8 < T < 14$ in a field centred on TIC-188620407.

magnitude (m) using the following equation:

$$m = z_p + 2.5\log(G) - 2.5\log\left(\frac{f}{t_{exp}}\right), \quad (3)$$

where z_p is the photometric zeropoint, G is the conversion factor from electrons to digital units G ($e^- ADU^{-1}$) as listed in Table 1, and t_{exp} the exposure time of the image. The zeropoint for the NGTS filter is determined by measuring the source flux of each star (in electrons) and comparing it to the known *TESS* magnitude of the star. Using the noise calculations and the conversion from flux to magnitude, we plot both the individual noise components and the total noise model in Fig. 4.

4.5 Systematic noise

All of the noise sources set out in Section 4 produce uncorrelated (white) noise. However it is well known that usually there is some level of systematic noise in the photometry that will give rise to correlated (red) noise (F. Pont, S. Zucker & D. Queloz 2006).

To quantify this, we test both cameras for correlated noise as a function of time. We bin the data at different time-scales to examine the noise characteristics. J. McCormac et al. (2017) demonstrated that NGTS photometry using the iKon-M CCDs showed very little red noise, as the majority of its contribution was mitigated by correcting for atmospheric extinction based on the airmass as well as the colour-dependent atmospheric extinction using `SysRem` python software (O. Tamuz, T. Mazeh & S. Zucker 2005).

We calculate the RMS of the light curves from unbinned cadence all the way up to 1800 s binning cadence, and compare the values to the square-root N value expected for purely white noise (see Section 5.2).

5 RESULTS

5.1 Noise model comparison

To assess the on-sky performance of the cameras, we compared measured noise characteristics to the theoretical noise model, which includes read noise, dark current, sky background noise, target shot noise, and scintillation noise (see Section 4.4).

Read noise and dark current are calculated using each camera's performance specifications (see Section 1). To model the sky background signal, we calculated the median value of all pixels for all bias and dark subtracted images taken on a particular observing night. This provides a good estimate of the sky background for nights when the sky background is not significantly varying. For scintillation noise, we used the average airmass of

Downloaded from academic.oup.com/rasti/article/doi/10.1093/rasti/rzag022/8530553 by claudia Legler user on 03 November 2026

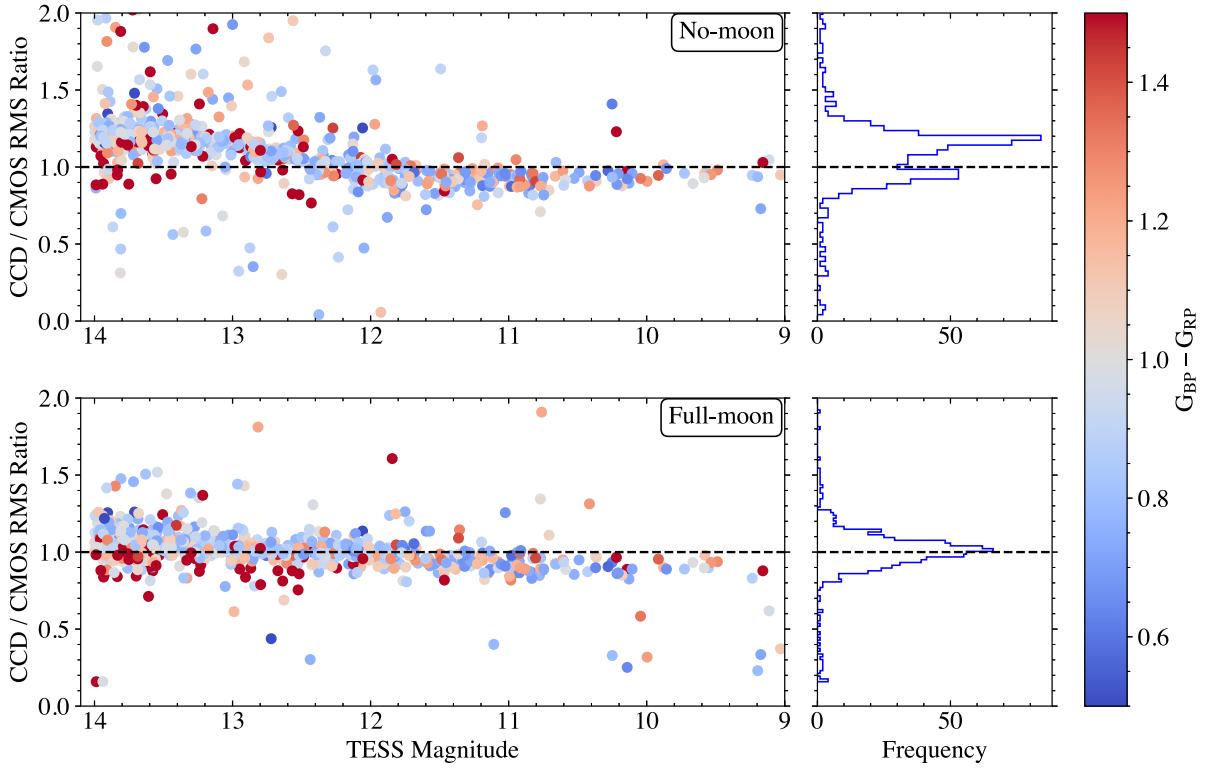


Figure 5. Ratio for CCD and CMOS camera noise contribution for different magnitude stars from Fig. 4. The data points are coloured according to the catalogued *Gaia* DR3 $G_{BP} - G_{RP}$ colour. The black dashed line represents the ratio 1 which is the case where the noise is the same for both cameras. *Top:* The noise ratio for a dark night (no-moon). *Bottom:* The noise ratio for a bright night (full-moon). The panels on the right show the histogram distributions.

the total observation and included locational parameters specific to the NGTS observatory (see Section 4.3). Finally, we created a synthetic flux array to calculate the shot noise, normalizing all noise parameters with respect to that flux. We measured the zeropoint from the fluxes extracted from photometry and their corresponding *TESS* magnitudes. The zeropoint was used as in equation (3) in order to convert to synthetic magnitudes. The total noise is the summation in quadrature of all the noise components as shown in equation (2).

For our noise model comparison, we acquired a set of data of the same field (R.A.$= 23^{h}20^{m}12^{s}.37$, Dec$= -13^{\circ}5'56''.83$) for a total of 5.5 h on the night of 2024 June 22 (full moon) and on the night of 2024 July 5 (no moon). Moon conditions were selected in order to assess the performance of each camera with maximum and minimum sky background contribution. We employed relative photometry for stars as described in Section 3.3 on a *TESS* magnitude range of $8 < T < 14$, with the same size physical photometric aperture for each camera (see the introduction of Section 4). This photometric aperture radius was found to be $\approx 2.9 \times$ FWHM ($1 \times$ FWHM $= 19.3\,\mu$m), which equates to a radius of 4 pixels for the CCD and 5 pixels for the CMOS (S. B. Howell 2000).

For each star we calculated the fractional RMS from the relative normalized light curves. The results for the data sets are shown in the upper panels (no moon) and lower panels (full moon) of Fig. 4. We colour code the RMS of each star with the *Gaia* DR3 $G_{BP} - G_{RP}$ colour to check RMS for a colour dependence.

The RMS distribution of the stars is in good agreement with the calculated total noise model for both cameras and both data sets. In all cases we see that that reddest stars have a slightly higher RMS than bluer stars. This is likely to be due to the fact that we are plotting the *TESS* magnitudes for these stars (600–1000 nm), but our photometry is in the NGTS band (520–890 nm). The difference between these bandpasses means that redder stars appear brighter in the *TESS* filter compared with the NGTS filter, which does not include wavelengths beyond 890 nm. Consequently, in Fig. 4, the reddest stars would appear brighter using their *TESS* magnitudes, and fainter for our NGTS photometry. Thus, these redder stars have slightly higher RMS. Our relative photometry and detrending methods are also optimized for the average colour star in the field, which will be much bluer than these very red stars. This could also result in systematics in the light curves of the redder stars which would produce higher RMS.

To directly compare the RMS for given stars as simultaneously observed in each camera, we plot the ratio of CCD RMS to CMOS RMS for each star, as shown in Fig. 5. When this RMS ratio exceeds unity, the RMS of the star is lower in the CMOS camera than in the CCD camera – i.e. the CMOS camera shows better precision in the light curve. Again we colour-code each star using its *Gaia* DR3 $G_{BP} - G_{RP}$.

5.2 Time-scale of noise

In order to investigate the presence of red noise in our data from each camera, we calculate the RMS for each light curve over a range of binning time-scales for the observations taken with no moon (2024 July 5). We trim the beginning and end of each night's data to include only observations taken at airmass < 1.7. This helps minimize excess noise associated with high airmass (E. M. Bryant et al. 2020), while retaining enough data for effective binning. The total usable data amounted to approximately 4.8 h.

Downloaded from academic.oup.com/rasti/article/doi/10.1093/rasti/rzag022/8530553 by claudia Legler user on 03 November 2026

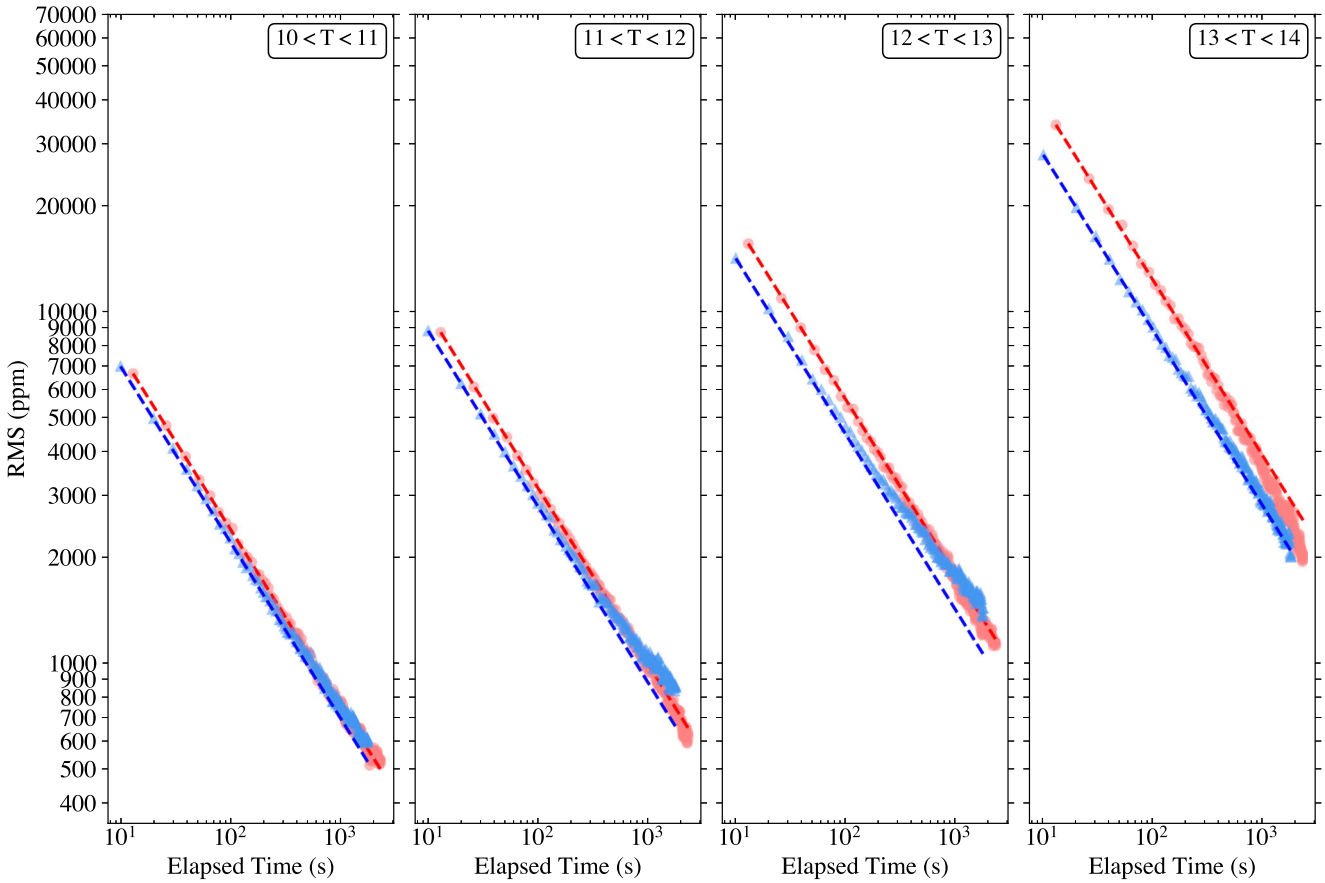


Figure 6. Noise levels for CCD (light red circles) and CMOS (light blue triangles) at varying time-scales during observations conducted on the no-moon night of 2024 July 5. The data is binned as a function of exposure and readout times. The blue and red dashed lines indicate the white noise model, proportional to $1/\sqrt{n}$ for the CMOS and CCD, respectively. The RMS noise was measured from stars that are non-variable and non-saturated. For the CMOS camera, 45 stars were randomly selected and averaged in each magnitude regime, and the same stars were used for the CCD camera.

Stars were grouped in 1 *TESS* magnitude intervals, and their RMS was averaged and plotted for each camera, as illustrated in Fig. 6. The maximum binning duration applied was 30 min. For each magnitude range, 45 stars were randomly selected, and the same set of stars was used for both cameras to ensure consistency. Each bin accounts for both the exposure, read and dead times. The exposure time was 10 s for both cameras, while the readout times differed. For the CMOS camera the readout time is 42 ms and we consider this negligible in our calculations. The CCD has a total of 3 s read and dead time (see Section 2.2).

For the first two magnitude ranges, $10 < T < 11$ and $11 < T < 12$, the RMS values for both cameras are comparable, with the CCD camera exhibiting slightly lower noise, as also illustrated in Fig. 5. In both cases, the RMS decreases similarly with binning time, following the expected trend from the white noise model. In the fainter magnitude bins, $12 < T < 13$ and $13 < T < 14$, the initial RMS for the CMOS camera is lower than that of the CCD camera, consistent with the relative performance indicated by the RMS ratio in Fig. 5.

5.3 Transit light curves

A total of 11 successful nights of simultaneous observations of eight well-known exoplanets transiting bright stars were conducted using the CMOS and CCD cameras, as summarized in Table 2. Relative photometry, as outlined in Section 3.3, was employed to detrend the light curves from systematic effects. For each target star, an exclusion criterion was applied to remove comparison stars exhibiting high noise levels or significant systematics.[6]

We applied additional detrending to all 11 of our target light curves using `allesfitter`, a `Python` package (M. N. Günther & T. Daylan 2019, 2021). To sample the parameters, we employ detrending using Gaussian Process on a covariance function, the Matern 3/2 kernel. The parameters are the characteristic amplitude $ln(\sigma)$ and length $ln(\rho)$ of scale.

To model the transits, `allesfitter` package integrates several specialized libraries such as `ellc` (P. F. L. Maxted 2016) for light-curve modelling, `dynesty` (J. S. Speagle 2020) for nested sampling (J. Skilling 2004; J. Skilling 2006) and `celerite` for Gaussian processes (D. Foreman-Mackey et al. 2017).

The eight transiting exoplanet systems that we observed have already been extensively observed and characterized with high-precision data from both ground- and space-based instruments. Therefore we chose to fit a photometric model using nested sampling of the initial parameters with their uncertainties adopted from the most up-to-date existing literature as listed on the NASA exoplanet archive for each system (R. L. Akeson et al. 2013). We

[6] https://github.com/EMBryant/bsproc

Downloaded from academic.oup.com/rasti/article/doi/10.1093/rasti/rzag022/8530553 by claudia Legler user on 03 November 2026

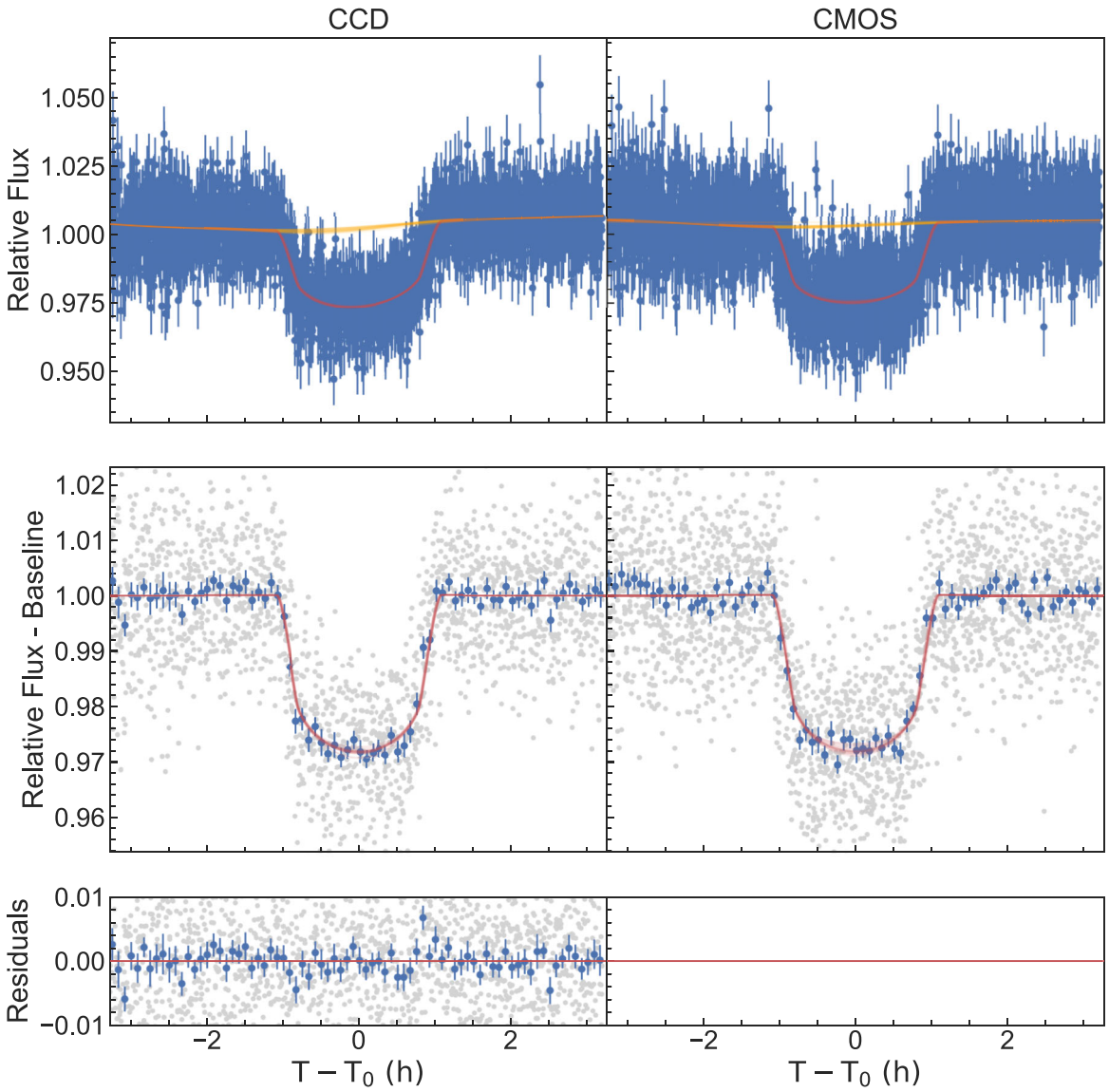


Figure 7. Normalized light curves for the transiting system of WASP-4 (TIC 402026209) from NGTS on 2024 August 2 for CCD (*left*) and CMOS *right*) cameras.*Top*: Undetrended light curves with the GP detrending function shown as yellow solid line and transit model shown with red solid line. *Middle*: Detrended light curve with data binned to 5 min (solid blue circles) for clarity. Again the best-fitting model is shown in red. *Bottom*: Residuals from the best fit.

used normal priors for orbital period P, the radius ratio (R_B/R_A), semimajor axis ($(R_A + R_B)/a$), the epoch ($T_{0,B}$), orbital inclination ($\cos i_B$), and the quadratic limb darkening coefficients calculated based on the effective temperature, metallicity and the logarithm surface gravity ($\log(g)$ of the host star; D. K. Sing 2010). The eight selected exoplanet system were all hot Jupiters with circular orbits reported in the literature. Therefore we set the eccentricity and argument of periastron of the system (implemented as the terms $\sqrt{e}\cos\omega$ and $\sqrt{e}\sin\omega$) as zero. All prior parameters were set to be the same for both the CCD and the CMOS cameras' extracted light curves. We did not include a dilution factor, as all the target stars are well isolated from nearby bright objects.

The results for the CCD and CMOS cameras' extracted light curves are plotted in Fig. 7 for WASP-4 with the fitted parameters in Table 3 and in Appendix A as Figs A1 to A10 and Table A1 to A10 for all other targets. The upper panels in Fig. 7 display the normalized light curves as extracted from the relative photometry and the detrending fit, the middle panels show the transit fit and the lower panels the residuals from the model. For plotting purposes we bin the detrended and model fitted light curves to 5 min bins (for both cameras) as shown in Fig. 7.

6 DISCUSSION

6.1 Fractional noise

The RMS precision for light curves generated from the CMOS images agree well with our noise model for instrumentation, sky background, and atmospheric scintillation noise (see right-hand panels in Fig. 4). The CCD data are also in good agreement with the noise model (see left-hand panels in Fig. 4).

We note that for the CMOS camera, the purely instrumental noise factors (dark current and read noise) are never a significant

Downloaded from academic.oup.com/rasti/article/doi/10.1093/rasti/rzag022/8530553 by claudia Legler user on 03 November 2026

Table 3. allesfitter model priors and fitted values. Planetary System properties for the transiting system WASP-4 (TIC 402026209), as shown in Fig. 7.

Parameter	Initial guess	Prior	Fitted value CMOS	Fitted value CCD
$R_p/R_\star$	0.15201	$\mathcal{N}(0.15201, 0.00040)$	0.15211 ± 0.00039	0.15215 ± 0.00039
$(R_\star + R_b)/a_b$	0.211339	$\mathcal{N}(0.211339, 0.002017)$	0.2122 ± 0.0016	0.2105 ± 0.0017
$\cos i_b$	0.016405	$\mathcal{N}(0.016405, 0.014657)$	$0.013^{+0.012}_{-0.013}$	$0.016^{+0.013}_{-0.014}$
Tc (BJD)	2455804.515752	$\mathcal{N}(2455804.515752, 0.000019)$	$2460525.796300 \pm 0.000080$	$2460525.796306 \pm 0.000079$
Orbital Period (d)	1.338231466	$\mathcal{N}(1.338231466, 0.000000023)$	$1.338231464 \pm 0.000000023$	$1.338231467 \pm 0.000000023$
q_1	0.385	$\mathcal{N}(0.385, 0.012)$	0.386 ± 0.012	0.387 ± 0.012
q_2	0.400	$\mathcal{N}(0.400, 0.087)$	$0.363^{+0.069}_{-0.075}$	0.419 ± 0.074

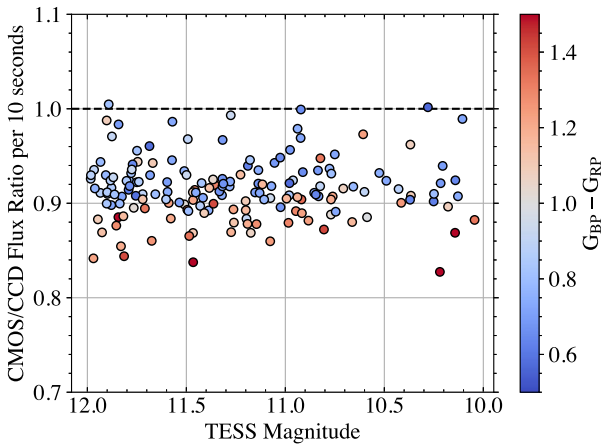


Figure 8. The CMOS/CCD flux ratio for a set of stars from the night of 2024 July 5. Flux ratios are represented by circles, colour-coded according to the catalogued *Gaia* DR3 $G_{BP} - G_{RP}$ colour. The dashed line represents the ratio 1 which is the case where the detected flux is equal for both cameras.

noise source, even for faint stars on nights with no moon. For the CCD camera, however, the read noise is at the same level as the sky background during no-moon conditions for stars fainter than T>13 mag. This difference is primarily due to the fact that the CCD camera has much higher read noise than the CMOS camera (see Table 1). This difference in read noise arises because CMOS pixels are read out in parallel, allowing the amplifiers to process signals at significantly lower frequencies. In contrast, CCD cameras have fewer amplifiers, requiring them to operate at higher frequencies, which leads to larger read noise (N. Teranishi & N. Mutoh 1986; J. Hynecek 1997; I. Apergis et al. 2025).

Although the dark current and amplifier glow contributions for the CMOS image sensors are much higher than the CCD image sensors (P. Qiu et al. 2021; S. Karpov et al. 2021; I. Apergis et al. 2025), the dark current is not a significant noise source even for the CMOS camera for this photometry. For the CMOS camera, observations of bright stars under no-moon conditions, we are either limited by atmospheric scintillation or photon shot noise from the target star. For fainter stars, photometric precision is limited by sky background noise, primarily due to the large pixel scale (4 arcsec pix^{-1}) and the point-spread function (FWHM = 1.7 pix). This limitation can be mitigated by reducing the photometric aperture size, which helps exclude excess background signal and improves signal-to-noise for fainter stars. We note that if there was a much finer pixel scale and narrower point-spread-function, then the sky contribution would be much less and therefore the dark current would start to become the dominant noise contribution for objects fainter than approximately T= 15 mag. During full-moon conditions, the increased sky background means that all stars with T> 10.5 mag will be limited by sky noise. This is also the case for the CCD camera.

We observed a distinct increase in the RMS for the very brightest stars (T< 9.5 mag) for the CMOS camera, which was less pronounced for the CCD camera (see Fig. 4). This effect is due to the saturation of the pixel's capacity of the CMOS camera and it is avoided by reducing the exposure time. The CMOS architecture is equipped with transistors within each pixel that amplify and convert charge to voltage. This process involves transferring charge from the photodiode by applying a specific voltage to the gate, which serves as an anti-blooming mechanism, preventing the escape of charge to adjacent pixels (K. D. Stefanov 2022; I. Apergis et al. 2025). The overall result of this is that charge is not conserved for saturated pixels, hence any relative photometry of a star with a saturated pixel will have a higher RMS proportional to the degree of saturation. A saturated star will not exhibit the same flux–airmass correlation as unsaturated stars, because its recorded counts are clipped by the pixel full well capacity rather than tracking the true incident flux. As a result, standard airmass-based detrending becomes ineffective for such targets, and applying it can introduce additional scatter into the light curve. This is evidenced by the increasing RMS with *TESS* magnitude for stars with T> 9 mag in Fig. 4. Although the CCD camera also saturates, the CCD photometry is more precise for these very bright stars. This is due to the sensor architecture of CCD cameras, whereby if a pixel exceeds its full well depth, the excess charge spreads to neighbouring pixels (J. R. Janesick et al. 1987). This results in bleeding or smearing artefacts, typically along the direction of charge transfer of the readout (J. R. Janesick et al. 1987). For very bright stars, these effects were evident in the CCD frames. In some cases, saturated pixels leaking charge into nearby pixels within the aperture can still be used for photometry, as demonstrated by B. J. S. Pope et al. (2016).

Both cameras demonstrate performance that aligns well with the noise model under both no-moon and full-moon sky conditions, achieving scintillation-limited performance for the brightest stars.

Upon analysing the noise ratio comparison shown in Fig. 5, we find that the CCD camera exhibits lower noise for bright stars ($10 < T < 12$). In this regime, the photon shot noise from the target stars dominates, and the CCD receives more signal than the CMOS for the same 10-s exposure. This behaviour arises because the NGTS filter is optimized for the CCD's quantum efficiency response. In contrast, the CMOS sensor, which is more sensitive to bluer wavelengths, operates with reduced efficiency since the NGTS filter cuts off much of its most sensitive spectral region (see Fig. 1). To demonstrate this, we plot the ratio of the average fluxes of catalog stars as a function of stellar effective temperature, as shown in Fig. 8. In this example, we consider only the

Downloaded from academic.oup.com/rasti/article/doi/10.1093/rasti/rzag022/8530553 by claudia Legler user on 03 November 2026

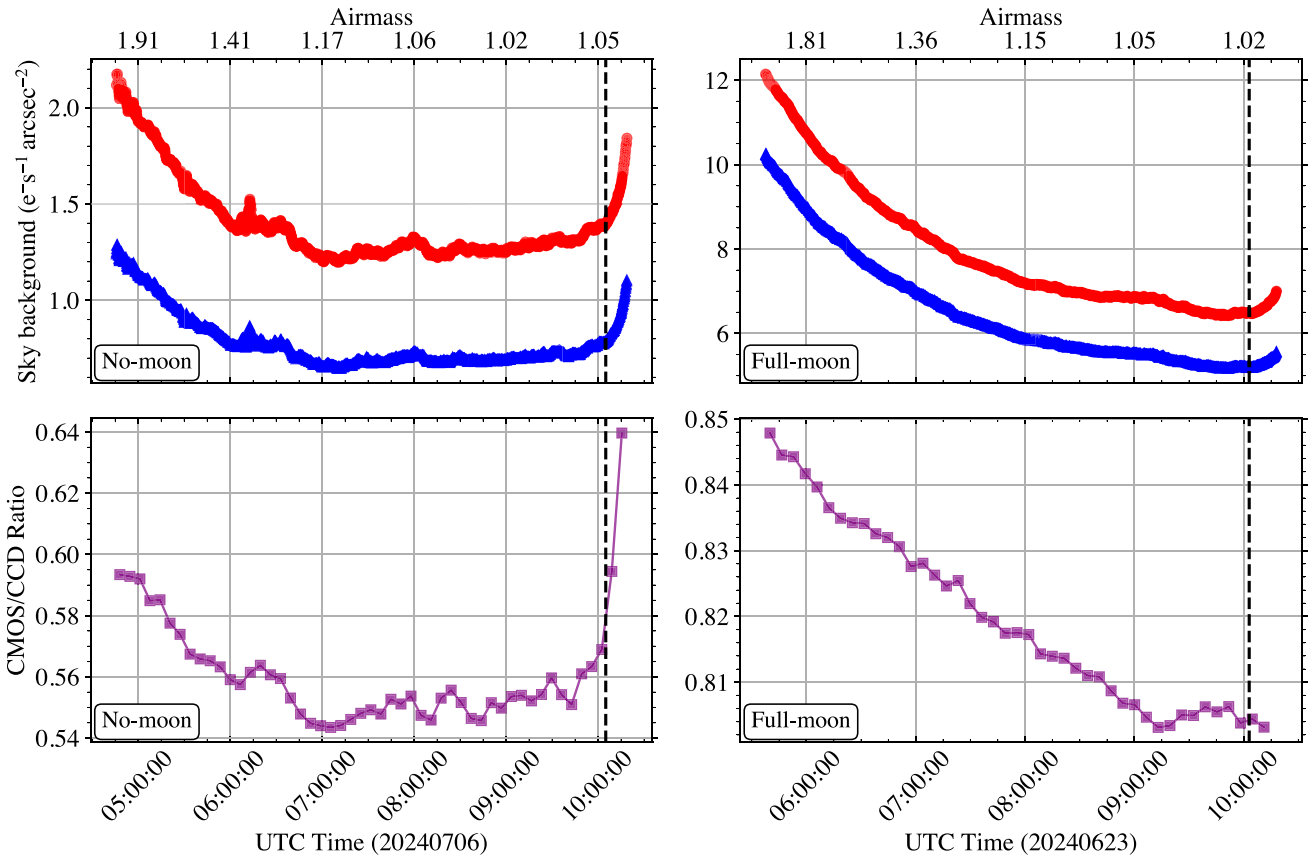


Figure 9. *Top:* Sky background flux (e^- pixel^{-1} arcsec^{-2}) as a function of time and airmass from the night of 2024 July 5 (*left*) and the night of 2024 June 22 (*right*) for the CMOS (blue triangles) and CCD (red circles). The dashed vertical line at UT10:05:00 (*left*) and UT10:03:00 (*right*) indicates the start of astronomical twilight. *Bottom:* The CMOS/CCD ratio of the fluxes from the top panel as a function of time.

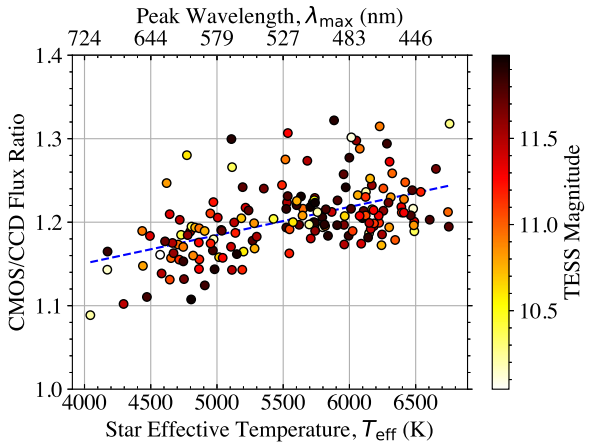


Figure 10. Ratio of the flux for bright stars ($T < 12$ mag), plotted against stellar effective temperature and corresponding peak wavelength, assuming each star behaves as a blackbody, as measured by the CMOS and CCD cameras from the night of 2024 July 5. Flux ratios are represented by circles, colour-coded according to *TESS* magnitude. The blue dashed line is best-fit linear model the data.

exposure times and do not account for duty cycles (see Fig. 10 for the full comparison). We find that the CCD consistently records higher flux values than the CMOS camera, with the mean ratio of CMOS/CCD flux being approximately 0.9. We also see the expected colour dependence, with bluer stars showing a higher flux ratio due to the fact that the CMOS quantum efficiency is more blue sensitive (see Fig. 1).

A clear transition is observed beyond $T > 12$ mag, and the CMOS camera achieves better precision. A similar pattern is seen under full-moon conditions (lower panel of Fig. 5), although the ratio distribution peaks at approximately 0.95. The transition is likely due to the fact that the CCD camera is more sensitive to the sky background signal compared to the CMOS camera (see Fig. 3 and the discussion of the airglow later in Section 6.2). At the bright end ($T < 9$ mag), direct comparison becomes impractical due to CMOS saturation. It should be noted that the comparisons in Figs 4 and 5 are made per exposure, without accounting for cadence.

6.2 Sky background

As shown in Fig. 4, sky-background is the dominant noise source for both our CMOS and CCD photometry for stars with $T > 13$ mag in no-moon conditions and $T > 11$ mag in full-moon conditions (using our chosen source aperture size). The CCD camera is deep-depleted, with its quantum efficiency peaking at red wavelengths (see Fig. 1). This makes the CCD camera more sensitive to the strong emission lines redwards of 600 nm, such as those from atomic oxygen and OH produced in the mesosphere (T. Maihara et al. 1993). This phenomenon, commonly referred to as airglow (S. Noll et al. 2012), remains detectable

Downloaded from academic.oup.com/rasti/article/doi/10.1093/rasti/rzag022/8530553 by claudia Legler user on 03 November 2026

despite the NGTS having a cut-off at 890 nm. In contrast, the CMOS camera is less sensitive to red wavelengths and therefore less sensitive to airglow. This effect is evident when comparing simultaneous images of the sky background with the CMOS and CCD camera. For example, the target pixel frame in Fig. 3 shows the CCD camera to have a sky background count of 4.02 e^- s^{-1} arcsec^{-2}, where the CMOS camera's sky background count is only 2.52 e^- s^{-1} arcsec^{-2}.

To examine this effect further, we measured the sky background for both cameras over a 6-hour observation on the no-moon night of 2024 July 5 and on the full-moon night of 2024 June 22. We used the counts from the sky background map. The digital units were converted to electrons and normalised by the exposure time and sky pixel area in arcsec^{-2}. The sky background flux in units of e^- pixel^{-1} arcsec^{-2} is shown in Fig. 9 as a function of time. The measurements for the no-moon data set show that although both cameras have a similar trend with time across the observation block, the sky background flux for the CMOS camera is consistently lower than the CCD camera by a factor of approximately 0.5 (see lower panel of Fig. 9). In contrast, the measurements for the full-moon show the contribution of the moon light which follows the same trend for both cameras while the sky background has increased significantly. The CMOS camera is consistently lower than the CCD camera however the ratio has been increased by a factor of approximately 0.8 (see lower panel of Fig. 9). Given the only difference is the quantum efficiency of the cameras, the higher sky background for the CCD camera can be attributed to the fact that the sky is brighter in the red wavelengths due to the night sky emission, and therefore the sky background is higher for the more red-sensitive CCD camera.

We note that the overall trend seen for both cameras in Fig. 9 is due to the fact that the airmass is high ($z = 1.91$) at the start of the observations. That increase in amplitude just before the end of the observations is primarily due to the fact that we are observing at the astronomical twilight.

6.3 Camera efficiency

We compare the amount of flux collected per unit time for each camera, which takes into account the sum of the exposure times (10 s) and dead times (3 s for the CCD camera and 0.042 s for the CMOS camera). The flux collected is also dependent on the quantum efficiency of each camera (see Fig. 1), the NGTS bandpass (520–890 nm) and the stellar effective temperature. We assume that the throughput of each NGTS telescope is identical.

We focused only on stars brighter than $T < 12$ mag. Flux measurements for each star were obtained by aperture photometry using a constant physical photometric radius for the CCD and CMOS images (55 µm–20 arcsec). The duration is determined by the combined exposure and readout times of the respective camera. To evaluate the performance, we computed the ratio of flux in electrons per unit time between the two cameras and compare it to the stellar effective temperature of each observed star, as shown in Fig. 10.

Overall, the flux ratio between the CMOS and CCD cameras is always greater than unity, which shows that the CMOS camera collects more electrons per unit elapsed time than the CCD camera. This is primarily due to the fact that the CMOS camera reads out approximately 70 times faster than the CCD camera when including the dead times. We find a trend in the flux ratio with the effective temperature of the star derived from the TIC8 (K. G. Stassun et al. 2018) catalogue (see Fig. 10). This trend is due to the fact that the CMOS camera is more blue-sensitive in its quantum efficiency compared to the CCD camera (see Fig. 1). This means that the CMOS camera performs even better than the CCD camera for the bluest (hottest) stars. We do not detect any trend in the flux ratio with respect to the magnitude of the stars.

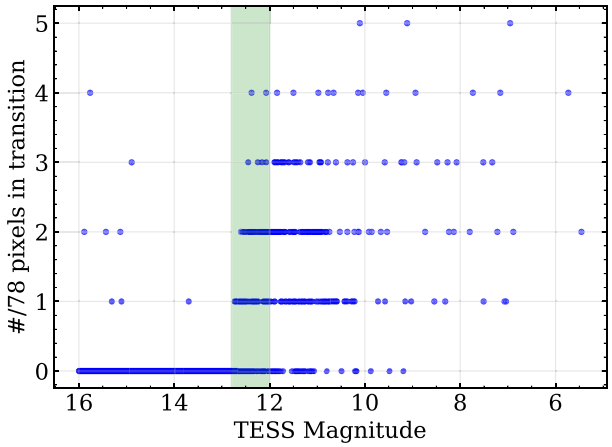


Figure 11. Number of transition pixels (1600–2000 ADU) inside the photometric aperture (∼78 pixels aperture) for a selection of stars observed with the CMOS camera on the night of 2024 July 5 (new moon conditions). The green shaded area represents the magnitude range in which transition pixels have the maximum value within the photometric aperture.

The Marana CMOS camera achieves an extended dynamic range through its HDR mode. In our previous work (I. Apergis et al. 2025), we demonstrated that a transition between the High Gain and Low Gain channels occurs at approximately ∼1800 ADU. Pixels with counts in this regime may be processed by either gain channel, thereby introducing additional noise (I. Apergis et al. 2025, see Fig. 9). We investigated which stars are affected by such transition pixels within their photometric apertures. We defined the transition region to be 1600–2000 ADU. For each star, we measured the number of pixels inside the aperture whose values fall within this range, and grouped stars into magnitude bins. This analysis is illustrated in Fig. 11.

Additionally, we identified stars for which the maximum pixel value inside the aperture, corresponding to the point spread function peak and contributing most significantly to the total flux, lies within the transition region. These stars were found to be in the range $12 < T < 12.8$, as indicated by the green shaded region in Fig. 11. The number of affected stars per magnitude bin, together with the average number of transition pixels per aperture for each star, is presented in Table A11. We also analysed the final relative photometry of stars whose point spread functions' contain transition pixels, and compared them with stars whose four highest pixel values do not include any transition pixels.

We find that for faint stars (T>13) there are no transition pixels in the photometric aperture. For stars brighter than T∼12 there are typically just a few transition pixels, and these pixels are not significantly contributing to the total flux measured for the star. Therefore in both these instances it is unlikely our photometric measurements will be affected by the transition feature of the CMOS detector. The magnitude $12 < T < 12.8$ is at highest risk of the photometry being affected by the CMOS transition from high gain to low gain channels. We do not find a noticeable increase in the of RMS noise of these light curves. However it would be advisable to ensure prime targets of photometric monitoring

Downloaded from academic.oup.com/rasti/article/doi/10.1093/rasti/rzag022/8530553 by claudia Legler user on 03 November 2026

are not in this region by selecting an appropriate exposure time for observations.

6.4 Red noise

Red noise is a critical limitation for many applications of bright star photometry – e.g. for detecting exoplanet transits (F. Pont et al. 2006). Our analysis of the photometric precision for the CMOS and CCD cameras at different time-scales (see Section 5.2 and Fig. 6) shows that the noise for both cameras is largely Gaussian (white) noise. This is as expected from previous analysis of NGTS bright star photometry (J. McCormac et al. 2017; P. J. Wheatley et al. 2018; E. M. Bryant et al. 2020; D. Bayliss et al. 2022; S. M. O'Brien et al. 2022).

7 CONCLUSIONS

The Marana CMOS camera was studied extensively on-sky at the Paranal Observatory using an NGTS telescope to test its suitability for high-precision photometry of exoplanet transits. We conducted simultaneous observations using a CCD camera to ensure exactly the same observing conditions and the same targets. The common exposure time was selected to be 10 s. We made sure we accounted for the difference in pixel size between the two cameras (13.5 versus 11 μm for the CCD and CMOS camera, respectively). We also considered the differences in the quantum efficiency when reaching our conclusions between the two cameras (Fig. 1).

The CMOS camera delivered photometry at the precision expected from our noise model, which was scintillation-limited for bright stars ($T < 11$ mag), and sky background-limited for fainter stars ($T > 13$ mag). In contrast to the CCD image sensor, the CMOS image sensor was never limited by readout noise. The CMOS camera's dark current noise is much higher than the CCD camera, but this was never a dominant source of noise for our photometry. We see minimal red noise contributions in the photometric precision of the CMOS camera, indicating there are no instrumental red-noise limitations using the CMOS camera for bright star photometry.

The fast readout of the CMOS camera (42 ms) enables a much higher duty cycle than the CCD camera. This effectively enables more flux to be collected over any given observing duration, and hence a better photometric precision. This is even true despite the slightly reduced quantum efficiency of the CMOS image sensor compared with the CCD image sensor, and the fact that the NGTS filter has been optimised to the CCD camera's quantum efficiency response. The transiting exoplanet light curves obtained using the CMOS camera are very similar to those obtained with the CCD camera. This result aligns well with other on-sky tests in the literature that show excellent photometric performance for CMOS cameras (S. Karpov et al. 2021; M. R. Alarcon et al. 2023).

In conclusion, we find that the Marana CMOS camera is suitable for high-precision time-series photometry. The fast readout speeds and low read noise and shutterless operation often provide a significant advantage over a traditional CCD camera. For applications requiring continuous imaging of rapidly varying astronomical targets, such as satellite tracking and mapping (B. F. Cooke et al. 2023; J. A. Blake et al. 2023; R. J. S. Airey et al. 2025), or near-Earth asteroid monitoring (S. M. Larson, G. R. Sims & E. J. Christensen 2018), CMOS image sensors offer distinct benefits. Furthermore, image degradation caused by saturated stars is mitigated in CMOS cameras due to their anti-blooming pixel architecture, reducing the risk of contamination to nearby targets of interest. As CMOS sensor technology continues to advance, it is likely that these cameras will replace CCDs in most astronomical time-series photometry applications.

ACKNOWLEDGEMENTS

This is a project based on the collaboration between the University of Warwick and Andor Technology Ltd under the STFC Industrial CASE (Cooperative Awards in Science and Technology) studentship. IA acknowledges the support of the UK Science and Technology Facilities Council (STFC) under the CASE Industry scheme (ST/W005077/1 Project title: Precision Photometry with the new generation of fast readout Scientific CMOS Camera). We acknowledge capital funding from the STFC Early Technology Development Capital Funding (ST/W005719/1 Project title: Discovering New Worlds with sCMOS Cameras). This work is based on data collected under the NGTS project at the ESO La Silla Paranal Observatory. The NGTS facility is operated by a consortium institutes with support from the UK Science and Technology Facilities Council (STFC) under projects ST/M001962/1, ST/S002642/1 and ST/W003163/1. JSJ gratefully acknowledges support by FONDECYT grant 1240738 and from the ANID BASAL project FB210003. ML acknowledges support of the Swiss National Science Foundation under grant number PCEFP2_194576. The contribution of ML has been carried out within the framework of the NCCR PlanetS supported by the Swiss National Science Foundation under grants 51NF40_182901 and 51NF40_205606. SMO is supported by a UK Science and Technology Facilities Council (STFC) Studentship (ST/W507751/1).

CONFLICT OF INTEREST

The authors declare no conflict of interest.

DATA AVAILABILITY

The software used is publicly available on the GitHub repository: https://github.com/AperpieGG/ngcmos. The full photometric data set from NGTS will be available upon request to the author.

REFERENCES

Aberle A. G., Glunz S. W., Warta W., 1992, J. Appl. Phys., 71, 4422
Airey R. J. S. et al., 2025, preprint (arXiv:2502.12324)
Akeson R. L. et al., 2013, PASP, 125, 989
Alarcon M. R., Licandro J., Serra-Ricart M., Joven E., Gaitan V., de Sousa R., 2023, PASP, 135, 055001
Anderson D. R. et al., 2011, ApJ, 726, L19
Apergis I. et al., 2025, RAS Techn. Instrum., 4, rzaf049
Barbary K., 2016, J. Open Source Softw., 1, 58
Battley M. P. et al., 2024, A&A, 686, A230
Bayliss D. et al., 2018, MNRAS, 475, 4467
Bayliss D. et al., 2020, The Messenger, 181, 28
Bayliss D. et al., 2022, in Holland A. D., Beletic J., eds, Proc. SPIE Conf. Ser. Vol. 12191, X-Ray, Optical, and Infrared Detectors for Astronomy X. SPIE, Bellingham, p. 121911A
Bertin E., Arnouts S., 1996, A&AS, 117, 393
Blake J. A. et al., 2023, in Proc. Advanced Maui Optical and Space Surveillance (AMOS) Technologies Conference. American Astronautical Society, Maui, p. 77
Borucki W. J. et al., 2010, Science, 327, 977
Bryant E. M. et al., 2020, MNRAS, 494, 5872

Downloaded from academic.oup.com/rasti/article/doi/10.1093/rasti/rzag022/8530553 by claudia Legler user on 03 November 2026

Chote P. et al., 2025, Adv. Space Res., 76, 764
Cooke B. F., Chote P., Pollacco D., West R., Blake J. A., McCormac J., Airey R., Shrive B., 2023, Adv. Space Res., 72, 907
Davis A. B. et al., 2020, AJ, 160, 229
Foreman-Mackey D., Agol E., Ambikasaran S., Angus R., 2017, AJ, 154, 220
Ge J. et al., 2022, preprint (arXiv:2206.06693)
Gill S. et al., 2020a, MNRAS, 491, 1548
Gill S. et al., 2020b, MNRAS, 495, 2713
Gill S. et al., 2020c, ApJ, 898, L11
Gill S. et al., 2024, MNRAS, 533, 109
Gillen E. et al., 2020, MNRAS, 492, 1008
Günther M. N., Daylan T., 2019, Astrophysics Source Code Library, record ascl:1903.003
Günther M. N., Daylan T., 2021, ApJS, 254, 13
Hawthorn F. et al., 2024, MNRAS, 528, 1841
Hellier C. et al., 2014, MNRAS, 440, 1982
Henderson B. A. et al., 2024, MNRAS, 530, 318
Howell S. B., 1989, PASP, 101, 616
Howell S. B., 2000, Handbook of CCD Astronomy. Cambridge Univ. Press, Cambridge
Hynecek J., 1997, IEEE Trans. Electron Dev., 44, 1679
Jackman J. A. G., Wheatley P. J., West R. G., Gill S., Jenkins J. S., 2023, MNRAS, 525, 1588
Janesick J., Andrews J., Tower J., Grygon M., Elliott T., Cheng J., Lesser M., Pinter J., 2007, in Grycewicz T. J., Marshall C. J., Warren P. G., eds, Proc. SPIE Conf. Ser. Vol. 6690, Focal Plane Arrays for Space Telescopes III. SPIE, Bellingham, p. 669003
Janesick J. R., Elliott T., Collins S., Blouke M. M., Freeman J., 1987, Opt. Eng., 26, 692
Kajino F. et al., 2019, in Proc. 36th International Cosmic Ray Conference (ICRC2019). Madison, WI, USA, p. 525
Karpov S., Bajat A., Christov A., Prouza M., Beskin G., 2020, in Holland A. D., Beletic J., eds, Proc. SPIE Conf. Ser. Vol. 11454, X-Ray, Optical, and Infrared Detectors for Astronomy IX. SPIE, Bellingham, p. 114540G
Karpov S., Christov A., Bajat A., Cunniffe R., Prouza M., 2021, Rev. Mex. Astron. Astrof. Conf. Ser., 53, 190
Kuhn R. B. et al., 2016, MNRAS, 459, 4281
Lang D., Hogg D. W., Mierle K., Blanton M., Roweis S., 2010, AJ, 139, 1782
Larson S. M., Sims G. R., Christensen E. J., 2018, in Navarro R., Geyl R., eds, Proc. SPIE Conf. Ser. Vol. 10706, Advances in Optical and Mechanical Technologies for Telescopes and Instrumentation III. SPIE, Bellingham, p. 1116
Layden C. et al., 2025, preprint (arXiv:2502.00101)
Lou S. et al., 2023, IEEE Trans. Electron Dev.,
Ma C., Wang X., 2013, in Proc. Int. Image Sensor Workshop. International Image Sensor Society, Snowbird, Utah, p. 129. Available at: https://imagesensors.org/2013-international-image-sensor-workshop-iisw/
Mackay C. D., 1986, ARA&A, 24, 255
Maihara T., Iwamuro F., Yamashita T., Hall D. N. B., Cowie L. L., Tokunaga A. T., Pickles A., 1993, PASP, 105, 940
Maxted P. F. L., 2016, A&A, 591, A111
McCormac J., Pollacco D., Skillen I., Faedi F., Todd I., Watson C. A., 2013, PASP, 125, 548
McCormac J. et al., 2017, PASP, 129, 025002
McCormac J. et al., 2020, MNRAS, 493, 126
McGraw J., Zimmer P., Ackermann M., 2016, in Ryan S., ed., Proc. Advanced Maui Optical and Space Surveillance Technologies Conference. The Maui Economic Development Board, p. 24
Mitchell M. A. et al., 2026, MNRAS, 545, staf2100
Mu H.-Y., Fan Z., Zhu Y.-N., Zhang Y., Wu H., 2024, Res. Astron. Astrophys., 24, 055009
Noll S., Kausch W., Barden M., Jones A. M., Szyszka C., Kimeswenger S., Vinther J., 2012, A&A, 543, A92
O'Brien S. M. et al., 2022, MNRAS, 509, 6111
Osborn J., Föhring D., Dhillon V. S., Wilson R. W., 2015, MNRAS, 452, 1707
Pepper J., Gould A., Depoy D. L., 2004, in Holt S. S., Deming D., eds, AIP Conf. Ser. Vol. 713, The Search for Other Worlds. AIP, New York, p. 185
Pollacco D. L. et al., 2006, PASP, 118, 1407
Pont F., Zucker S., Queloz D., 2006, MNRAS, 373, 231
Pope B. J. S. et al., 2016, MNRAS, 455, L36
Qiu P., Zhao Y., Zheng J., Wang J.-F., Jiang X.-J., 2021, Res. Astron. Astrophys., 21, 268
Rauer H. et al., 2025, Exp. Astron., 59, 26
Ricker G. R. et al., 2015, J. Astron. Telesc. Instrum. Syst., 1, 014003
Rodel T. et al., 2025, MNRAS, 537, 35
Shockley W., Read W. T., 1952, Phys. Rev., 87, 835
Sing D. K., 2010, A&A, 510, A21
Skilling J., 2004, in Fischer R., Preuss R., Toussaint U. V., eds, AIP Conf. Ser. Vol. 735, Nested sampling. Am. Inst. Phys., New York
Speagle J. S., 2020, MNRAS, 493, 3132
Stassun K. G. et al., 2018, AJ, 156, 102
Stefanov K. D., 2022, CMOS Image Sensors. IOP Publishing, Bristol
Tamuz O., Mazeh T., Zucker S., 2005, MNRAS, 356, 1466
Tang X., Qian Y., Kong X., Wang H., 2020, J. Real-Time Image Proc., 17, 703
Teranishi N., Mutoh N., 1986, IEEE Trans. Electron Dev., 33, 1696
Ulmer-Moll S. et al., 2022, A&A, 666, A46
Wang S.-Y. et al., 2024, in Bryant J. J., Motohara K., Vernet J. R. D., eds, Proc. SPIE Conf. Ser. Vol. 13096, Ground-based and Airborne Instrumentation for Astronomy X. SPIE, Bellingham, p. 130962Y
Wang X., Ma C., Liu Y., Li Y., Zhou Q., 2015, in Proc. International Image Sensor Workshop. International Image Sensor Society, Vaals, the Netherlands
West R. G. et al., 2019, MNRAS, 486, 5094
Wheatley P. J. et al., 2018, MNRAS, 475, 4476
Wilson D. M. et al., 2008, ApJ, 675, L113
Wong I. et al., 2021, AJ, 162, 256
Wüst S., Bittner M., Espy P. J., French W. J. R., Mulligan F. J., 2022, Atmos. Chem. Phys. Disc., 2022, 1
Xiao K. et al., 2025, preprint (arXiv:2503.12449)
Yee S. W. et al., 2023, ApJS, 265, 1
Young A. T., 1967, AJ, 72, 747

APPENDIX A:

Downloaded from academic.oup.com/rasti/article/doi/10.1093/rasti/rzag022/8530553 by claudia Legler user on 03 November 2026

Table A1. `allesfitter` model priors. Planetary system properties for the transiting system TOI-905 (TIC 261867566) from NGTS on 2024 July 13.

Parameter	Initial guess	Prior	Fitted value CMOS	Fitted value CCD
$R_p/R_\star$	0.1311	$\mathcal{N}(0.1311, 0.0012)$	$0.1307^{+0.0011}_{-0.0012}$	0.1310 ± 0.0011
$(R_\star + R_b)/a_b$	0.102827	$\mathcal{N}(0.102827, 0.010844)$	0.1058 ± 0.0034	0.1026 ± 0.0034
$\cos i_b$	0.075327	$\mathcal{N}(0.075327, 0.004524)$	0.0784 ± 0.0032	$0.0734^{+0.0035}_{-0.0037}$
Tc (BJD)	2460505.6096463003	$\mathcal{N}(2460505.6096463, 0.0004719)$	$2460505.61003 \pm 0.00040$	$2460505.60988 \pm 0.00040$
Orbital period (d)	3.7395671	$\mathcal{N}(3.7395671, 0.0000013)$	$3.7395672^{+0.0000012}_{-0.0000013}$	3.7395670 ± 0.0000013
q_1	0.387	$\mathcal{N}(0.387, 0.015)$	0.389 ± 0.015	$0.388^{+0.014}_{-0.016}$
q_2	0.408	$\mathcal{N}(0.408, 0.099)$	0.447 ± 0.093	0.400 ± 0.097

Table A2. `allesfitter` model priors. Planetary system properties for the transiting system WASP-95 (TIC 144065872) from NGTS on 2024 July 14.

Parameter	Initial Guess	Prior	Fitted value CMOS	Fitted value CCD
$R_p/R_\star$	0.1025	$\mathcal{N}(0.1025, 0.0005)$	0.10231 ± 0.00055	$0.10250^{+0.00047}_{-0.00053}$
$(R_\star + R_b)/a_b$	0.172266	$\mathcal{N}(0.172266, 0.005922)$	$0.1771^{+0.0050}_{-0.0026}$	$0.1732^{+0.0057}_{-0.0048}$
$\cos i_b$	0.027922	$\mathcal{N}(0.027922, 0.036611)$	$0.019^{+0.028}_{-0.039}$	$0.048^{+0.017}_{-0.036}$
Tc (BJD)	2458553.711158	$\mathcal{N}(2458553.711158, 0.000088)$	$2460506.80136 \pm 0.00070$	$2460506.80373 \pm 0.00073$
Orbital period (d)	2.1846730	$\mathcal{N}(2.1846730, 0.0000014)$	$2.18467329^{+0.0000013}_{-0.00000090}$	$2.1846729^{+0.0000014}_{-0.0000013}$
q_1	0.357	$\mathcal{N}(0.357, 0.012)$	$0.359^{+0.012}_{-0.015}$	0.359 ± 0.011
q_2	0.393	$\mathcal{N}(0.393, 0.089)$	$0.366^{+0.060}_{-0.065}$	0.369 ± 0.079

Table A3. `allesfitter` model priors and fitted values. Planetary System properties for the transiting system TOI-2109 (TIC 392476080) from NGTS on 2024 July 17.

Parameter	Initial Guess	Prior	Fitted value CMOS	Fitted value CCD
$R_p/R_\star$	0.08155	$\mathcal{N}(0.08155, 0.00022)$	0.08155 ± 0.00022	0.08155 ± 0.00022
$(R_\star + R_b)/a_b$	0.476874	$\mathcal{N}(0.476874, 0.044155)$	0.4701 ± 0.0073	$0.4649^{+0.0080}_{-0.0076}$
$\cos i_b$	0.329855	$\mathcal{N}(0.329855, 0.006089)$	0.3297 ± 0.0060	0.3299 ± 0.0059
Tc (BJD)	2459378.455370	$\mathcal{N}(2459378.455370, 0.000059)$	$2460509.556868 \pm 0.000074$	$2460509.556874 \pm 0.000074$
Orbital period (d)	0.672474140	$\mathcal{N}(0.672474140, 0.000000028)$	$0.672474141 \pm 0.000000028$	$0.672474141^{+0.000000027}_{-0.000000029}$
q_1	0.305	$\mathcal{N}(0.305, 0.008)$	0.304 ± 0.008	0.305 ± 0.008
q_2	0.375	$\mathcal{N}(0.375, 0.074)$	0.379 ± 0.074	0.377 ± 0.074

Table A4. `allesfitter` model priors and fitted values. Planetary System properties for the transiting system KELT-10 (TIC 269217040) from NGTS on 2024 August 1.

Parameter	Initial guess	Prior	Fitted value CMOS	Fitted value CCD
$R_p/R_\star$	0.1190	$\mathcal{N}(0.1190, 0.0014)$	0.11793 ± 0.0010	0.12013 ± 0.0010
$(R_\star + R_b)/a_b$	0.119807	$\mathcal{N}(0.119807, 0.004107)$	$0.1212^{+0.0028}_{-0.0025}$	$0.1205^{+0.0025}_{-0.0023}$
$\cos i_b$	0.024258	$\mathcal{N}(0.024258, 0.015002)$	$0.021^{+0.011}_{-0.013}$	$0.017^{+0.010}_{-0.012}$
Tc (BJD)	2457612.49947	$\mathcal{N}(2457612.49947, 0.00041)$	2460524.7109 ± 0.0011	$2460524.7110^{+0.0010}_{-0.0011}$
Orbital Period (d)	4.1662541	$\mathcal{N}(4.1662541, 0.0000016)$	4.1662541 ± 0.0000016	4.1662541 ± 0.0000016
q_1	0.350	$\mathcal{N}(0.350, 0.010)$	0.349 ± 0.010	0.351 ± 0.010
q_2	0.385	$\mathcal{N}(0.385, 0.081)$	0.341 ± 0.069	0.416 ± 0.068

Downloaded from academic.oup.com/rasti/article/doi/10.1093/rasti/rzag022/8530553 by claudia Legler user on 03 November 2026

Table A5. `allesfitter` model priors and fitted values. Planetary System properties for the transiting system WASP-97 (TIC 230982885) from NGTS on 2024 August 04.

Parameter	Initial guess	Prior	Fitted value CMOS	Fitted value CCD
$R_p/R_\star$	0.1091	$\mathcal{N}(0.1091, 0.0009)$	0.10856 ± 0.00077	0.10913 ± 0.00079
$(R_\star + R_b)/a_b$	0.168300	$\mathcal{N}(0.168300, 0.003833)$	0.1686 ± 0.0035	$0.1699^{+0.0028}_{-0.0026}$
$\cos i_b$	0.034899	$\mathcal{N}(0.034899, 0.022665)$	$0.046^{+0.010}_{-0.013}$	$0.023^{+0.014}_{-0.017}$
Tc (BJD)	2458554.475352	$\mathcal{N}(2458554.475352, 0.000074)$	$2460527.74264 \pm 0.00020$	$2460527.74252 \pm 0.00021$
Orbital period (d)	2.07275965	$\mathcal{N}(2.07275965, 0.00000021)$	$2.07275967^{+0.00000020}_{-0.00000021}$	$2.07275965 \pm 0.00000021$
q_1	0.369	$\mathcal{N}(0.369, 0.009)$	0.369 ± 0.009	0.369 ± 0.009
q_2	0.400	$\mathcal{N}(0.400, 0.076)$	0.410 ± 0.068	0.389 ± 0.068

Table A6. `allesfitter` model priors and fitted values. Planetary system properties for the transiting system WASP-97 (TIC 230982885) from NGTS on 2024 August 06.

Parameter	Initial guess	Prior	Fitted value CMOS	Fitted value CCD
$R_p/R_\star$	0.1091	$\mathcal{N}(0.1091, 0.0009)$	0.10825 ± 0.00078	0.10865 ± 0.00079
$(R_\star + R_b)/a_b$	0.168300	$\mathcal{N}(0.168300, 0.003833)$	$0.1681^{+0.0033}_{-0.0031}$	0.1681 ± 0.0035
$\cos i_b$	0.034899	$\mathcal{N}(0.034899, 0.022665)$	$0.040^{+0.012}_{-0.016}$	$0.045^{+0.010}_{-0.014}$
Tc (BJD)	2458554.475352	$\mathcal{N}(2458554.475352, 0.000074)$	$2460529.81532 \pm 0.00020$	$2460529.81530^{+0.00019}_{-0.00020}$
Orbital period (d)	2.07275965	$\mathcal{N}(2.07275965, 0.00000021)$	$2.07275964 \pm 0.00000021$	$2.07275965 \pm 0.00000021$
q_1	0.369	$\mathcal{N}(0.369, 0.009)$	0.369 ± 0.009	0.369 ± 0.009
q_2	0.400	$\mathcal{N}(0.400, 0.076)$	0.385 ± 0.067	0.380 ± 0.070

Table A7. `allesfitter` model priors and fitted values. Planetary System properties for the transiting system WASP-95 (TIC 144065872) from NGTS on 2024 August 07.

Parameter	Initial guess	Prior	Fitted value CMOS	Fitted value CCD
$R_p/R_\star$	0.1025	$\mathcal{N}(0.1025, 0.0005)$	$0.10251^{+0.00036}_{-0.00059}$	0.10215 ± 0.00048
$(R_\star + R_b)/a_b$	0.172266	$\mathcal{N}(0.172266, 0.005922)$	0.1783 ± 0.0050	$0.1765^{+0.0055}_{-0.0051}$
$\cos i_b$	0.027922	$\mathcal{N}(0.027922, 0.036611)$	$0.031^{+0.029}_{-0.090}$	$0.051^{+0.016}_{-0.038}$
Tc (BJD)	2458553.711158	$\mathcal{N}(2458553.711158, 0.000088)$	$2460530.83412^{+0.00045}_{-0.00050}$	$2460530.83438 \pm 0.00056$
Orbital period (d)	2.1846730	$\mathcal{N}(2.1846730, 0.0000014)$	$2.1846731^{+0.0000010}_{-0.0000012}$	2.1846729 ± 0.0000014
q_1	0.357	$\mathcal{N}(0.357, 0.012)$	$0.354^{+0.008}_{-0.009}$	0.359 ± 0.012
q_2	0.393	$\mathcal{N}(0.393, 0.089)$	$0.446^{+0.065}_{-0.049}$	0.407 ± 0.079

Table A8. `allesfitter` model priors and fitted values. Planetary System properties for the transiting system KELT-10 (TIC 269217040) from NGTS on 2024 August 26.

Parameter	Initial guess	Prior	Fitted value CMOS	Fitted value CCD
$R_p/R_\star$	0.1190	$\mathcal{N}(0.1190, 0.0014)$	0.11958 ± 0.00099	$0.1167^{+0.0014}_{-0.0013}$
$(R_\star + R_b)/a_b$	0.119807	$\mathcal{N}(0.119807, 0.004107)$	$0.1204^{+0.0028}_{-0.0025}$	$0.1206^{+0.0033}_{-0.0031}$
$\cos i_b$	0.024258	$\mathcal{N}(0.024258, 0.015002)$	$0.022^{+0.010}_{-0.013}$	$0.0354^{+0.0090}_{-0.013}$
Tc (BJD)	2457612.49947	$\mathcal{N}(2457612.49947, 0.00041)$	$2460549.70892 \pm 0.00099$	2460549.7083 ± 0.0011
Orbital period (d)	4.1662541	$\mathcal{N}(4.1662541, 0.0000016)$	4.1662541 ± 0.0000016	4.1662541 ± 0.0000015
q_1	0.350	$\mathcal{N}(0.350, 0.010)$	0.350 ± 0.010	$0.350^{+0.010}_{-0.011}$
q_2	0.385	$\mathcal{N}(0.385, 0.081)$	0.358 ± 0.064	0.368 ± 0.072

Downloaded from academic.oup.com/rasti/article/doi/10.1093/rasti/rzag022/8530553 by claudia Legler user on 03 November 2026

Table A9. `allesfitter` model priors and fitted values. Planetary system properties for the transiting system TOI-4463 (TIC 8599009) from NGTS on 2024 August 27.

Parameter	Initial guess	Prior	Fitted value CMOS	Fitted value CCD
$R_p/R_\star$	0.11449	$\mathcal{N}(0.11449, 0.00397)$	$0.1154^{+0.0032}_{-0.0030}$	0.1133 ± 0.0039
$(R_\star + R_b)/a_b$	0.136414	$\mathcal{N}(0.136414, 0.004037)$	0.1360 ± 0.0029	0.1351 ± 0.0032
$\cos i_b$	0.107652	$\mathcal{N}(0.107652, 0.004857)$	0.1088 ± 0.0027	0.1107 ± 0.0031
Tc (BJD)	2459291.64004	$\mathcal{N}(2459291.64004, 0.00032)$	$2460550.51237 \pm 0.00068$	$2460550.51468 \pm 0.00086$
Orbital period (d)	2.8807198	$\mathcal{N}(2.8807198, 0.0000028)$	$2.8807197^{+0.0000029}_{-0.0000027}$	2.8807198 ± 0.0000028
q_1	0.372	$\mathcal{N}(0.372, 0.007)$	0.372 ± 0.008	0.372 ± 0.008
q_2	0.400	$\mathcal{N}(0.400, 0.071)$	0.397 ± 0.070	$0.401^{+0.074}_{-0.069}$

Table A10. `allesfitter` model priors and fitted values. Planetary system properties for the transiting system WASP-30 (TIC 9725627) from NGTS on 2024 August 28.

Parameter	Initial guess	Prior	Fitted value CMOS	Fitted value CCD
$R_p/R_\star$	0.0705	$\mathcal{N}(0.0705, 0.0011)$	0.0728 ± 0.0010	0.06924 ± 0.0010
$(R_\star + R_b)/a_b$	0.121078	$\mathcal{N}(0.121078, 0.001989)$	0.1250 ± 0.0015	0.1233 ± 0.0019
$\cos i_b$	0.007505	$\mathcal{N}(0.007505, 0.008202)$	0.0042 ± 0.0063	0.0053 ± 0.0076
Tc (BJD)	2460551.738836	$\mathcal{N}(2460551.738836, 0.0068717)$	2460551.7454 ± 0.0013	2460551.7421 ± 0.0026
Orbital period (d)	4.156736	$\mathcal{N}(4.156736, 0.00000202)$	4.1567360 ± 0.0000020	4.1567359 ± 0.0000020
q_1	0.330	$\mathcal{N}(0.330, 0.006)$	0.329 ± 0.006	0.329 ± 0.006
q_2	0.373	$\mathcal{N}(0.373, 0.065)$	0.372 ± 0.065	0.350 ± 0.063

Table A11. Percentage ratio of transition pixels within star apertures.

TESS Magnitude bin	Stars affected by transition pixels	Average number of pixels in transition #/78
6–7	2/2	3.50
7–8	9/9	2.33
8–9	10/10	2.40
9–10	15/18	2.00
10–11	53/57	1.81
11–12	92/115	1.54
12–13	85/196	0.65
13–14	1/378	0.00
14–15	1/547	0.01
15–16	6/942	0.01

Downloaded from academic.oup.com/rasti/article/doi/10.1093/rasti/rzag022/8530553 by claudia Legler user on 03 November 2026

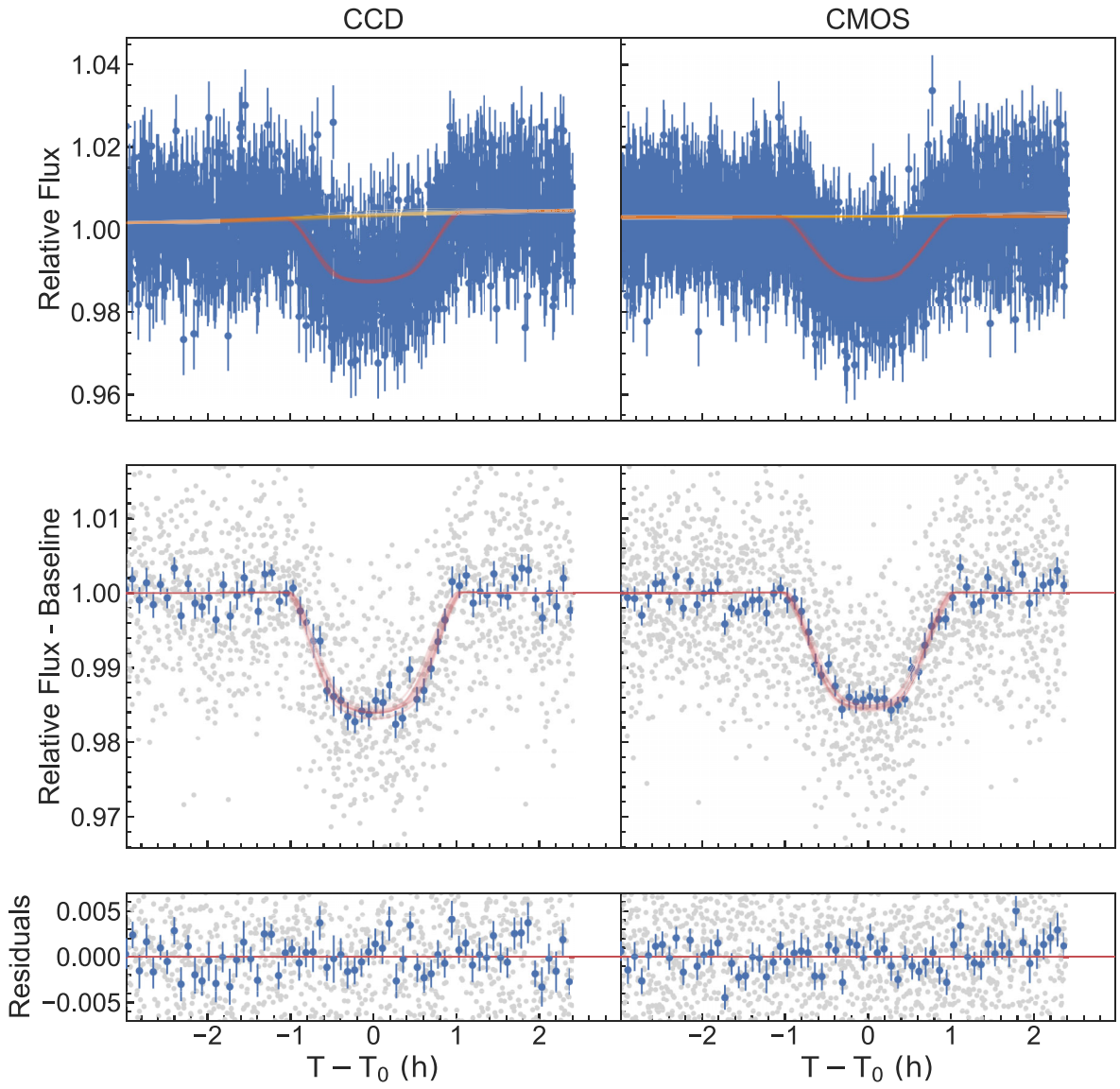


Figure A1. Same as in Fig. 7. Normalized light curves for the transiting system of TOI-905 (TIC 261867566) from NGTS on 2024 July 13.

Downloaded from academic.oup.com/rasti/article/doi/10.1093/rasti/rzag022/8530553 by claudia Legler user on 03 November 2026

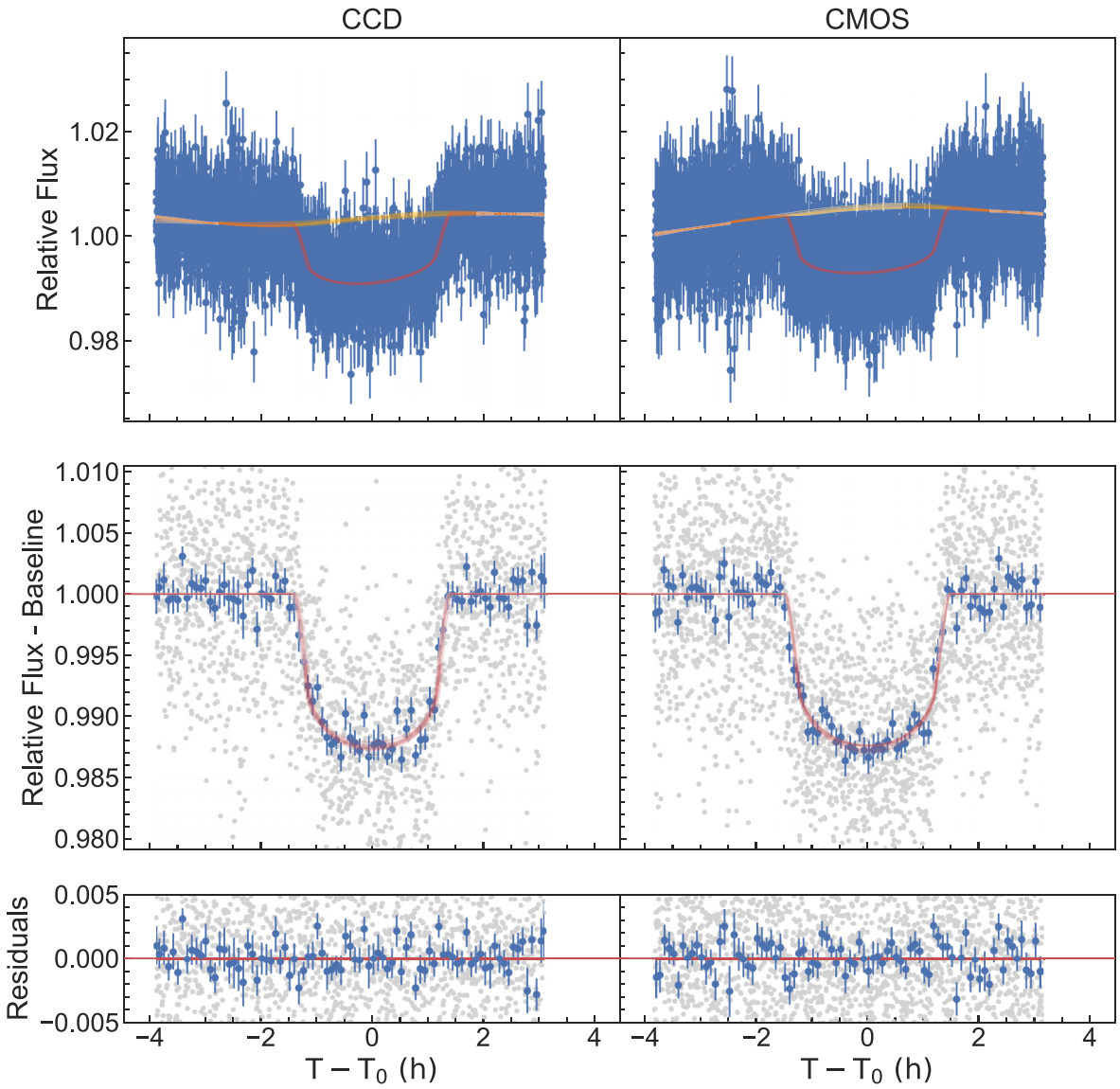


Figure A2. Same as in Fig. 7. Normalized light curves for the transiting system of WASP-95 (TIC 144065872) from NGTS on 2024 July 14.

Downloaded from academic.oup.com/rasti/article/doi/10.1093/rasti/rzag022/8530553 by claudia Legler user on 03 November 2026

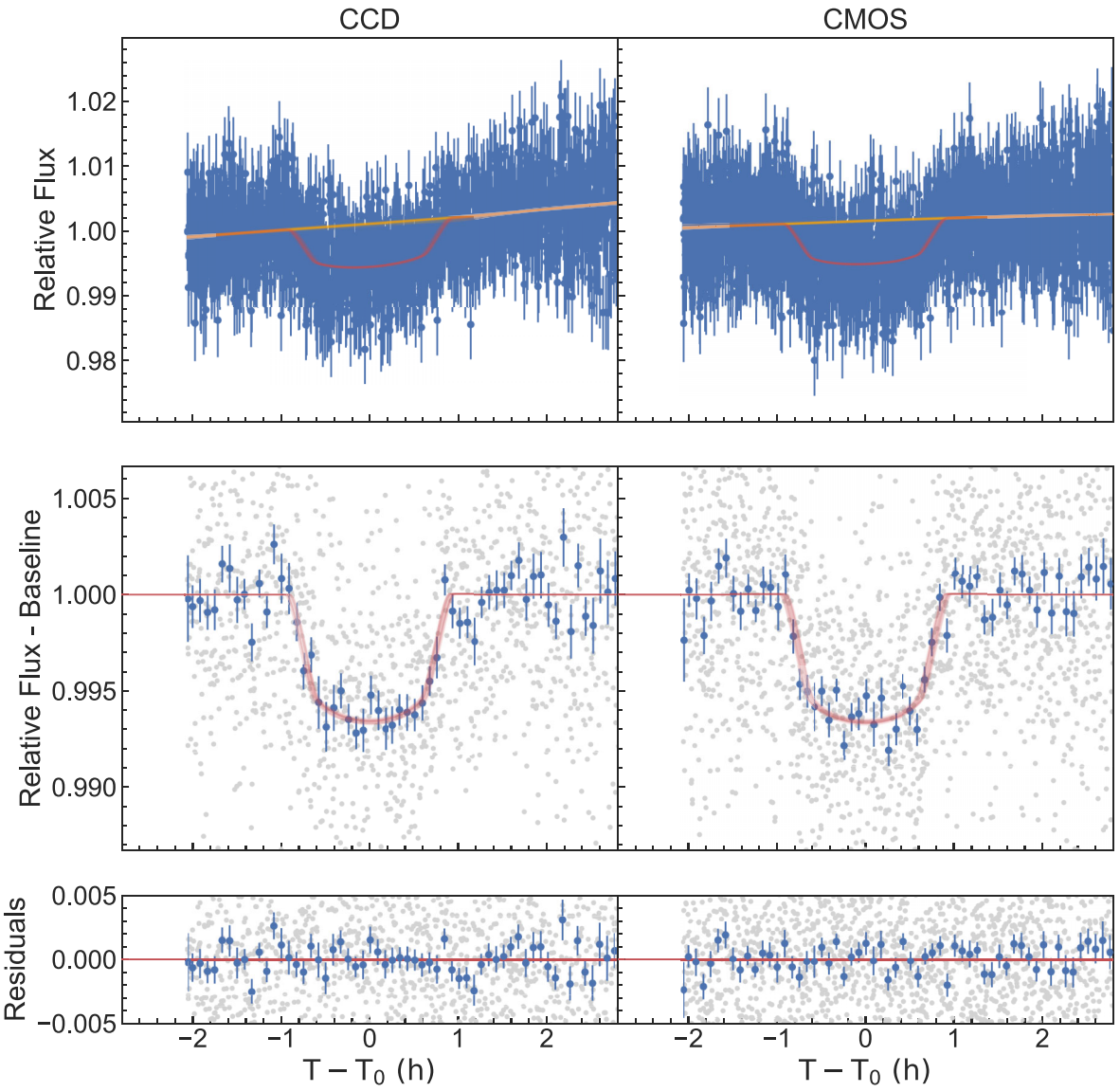


Figure A3. Same as in Fig. 7. Normalized light curves for the transiting system of TOI-2109 (TIC 392476080) from NGTS on 2024 July 17.

Downloaded from academic.oup.com/rasti/article/doi/10.1093/rasti/rzag022/8530553 by claudia Legler user on 03 November 2026

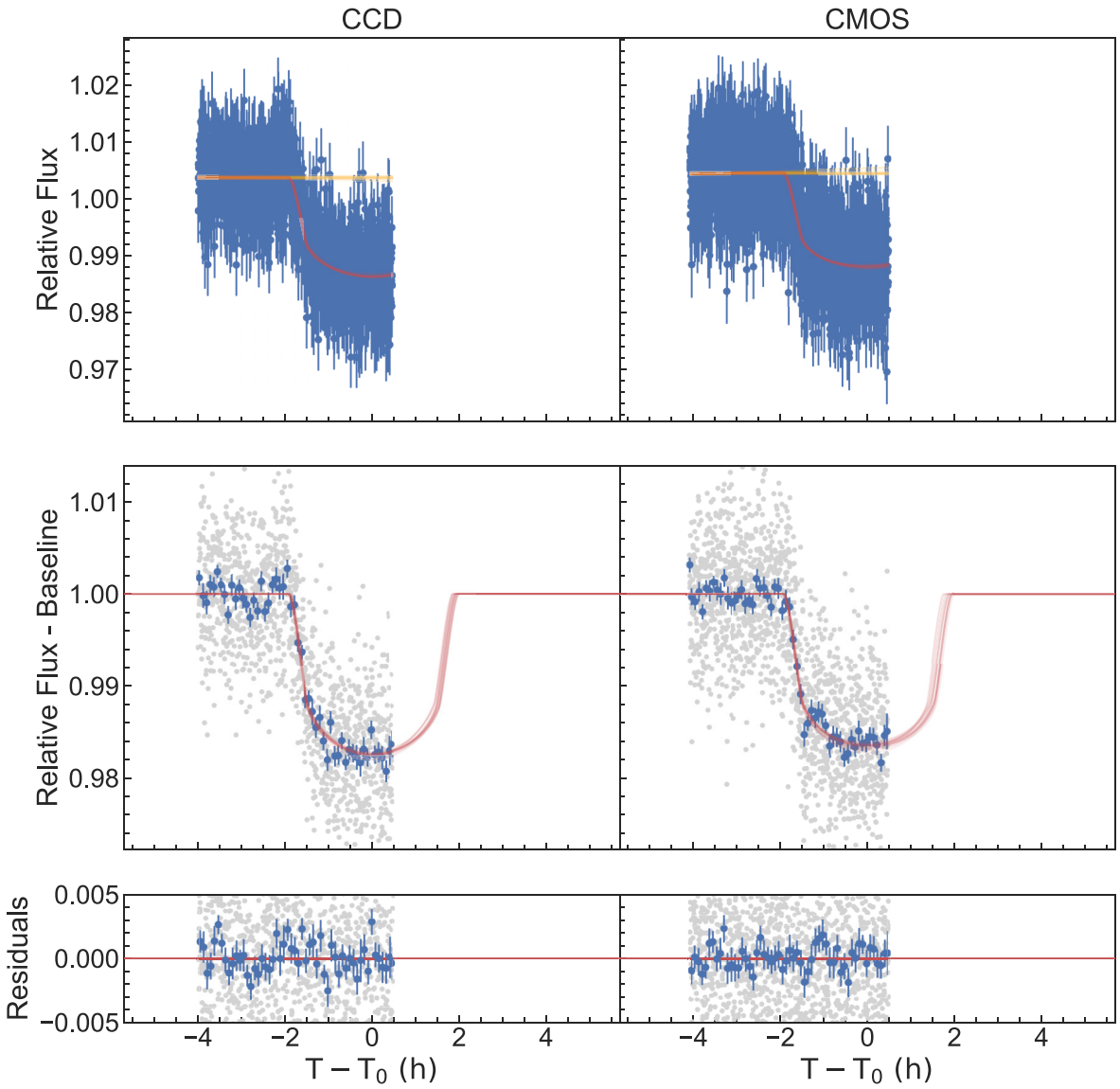


Figure A4. Same as in Fig. 7. Normalized light curves for the transiting system of KELT-10 (TIC 269217040) from NGTS on 2024 August 1.

Downloaded from academic.oup.com/rasti/article/doi/10.1093/rasti/rzag022/8530553 by claudia Legler user on 03 November 2026

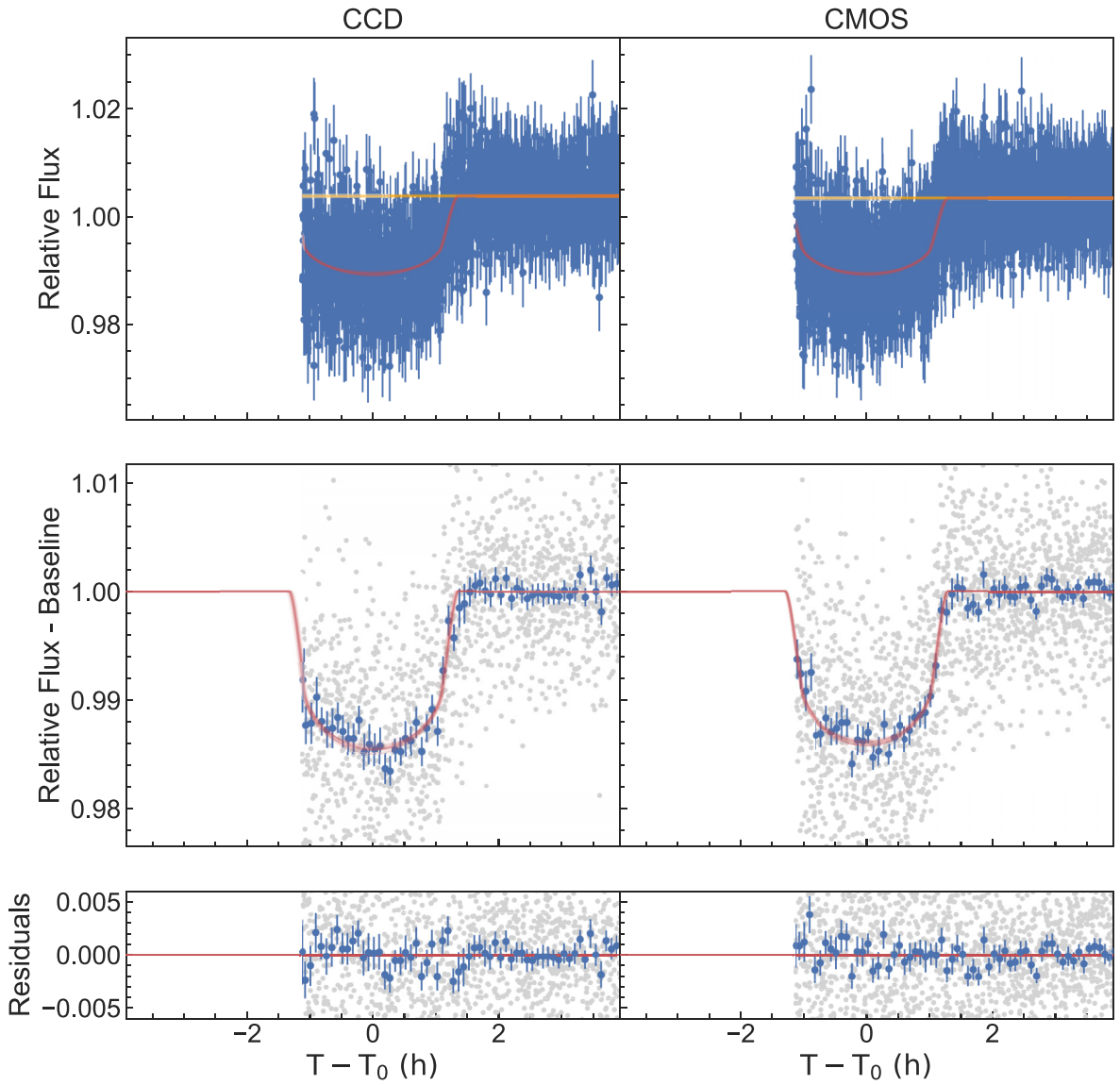


Figure A5. Same as in Fig. 7. Normalized light curves for the transiting system of WASP-97 (TIC 230982885) from NGTS on 2024 August 4.

Downloaded from academic.oup.com/rasti/article/doi/10.1093/rasti/rzag022/8530553 by claudia Legler user on 03 November 2026

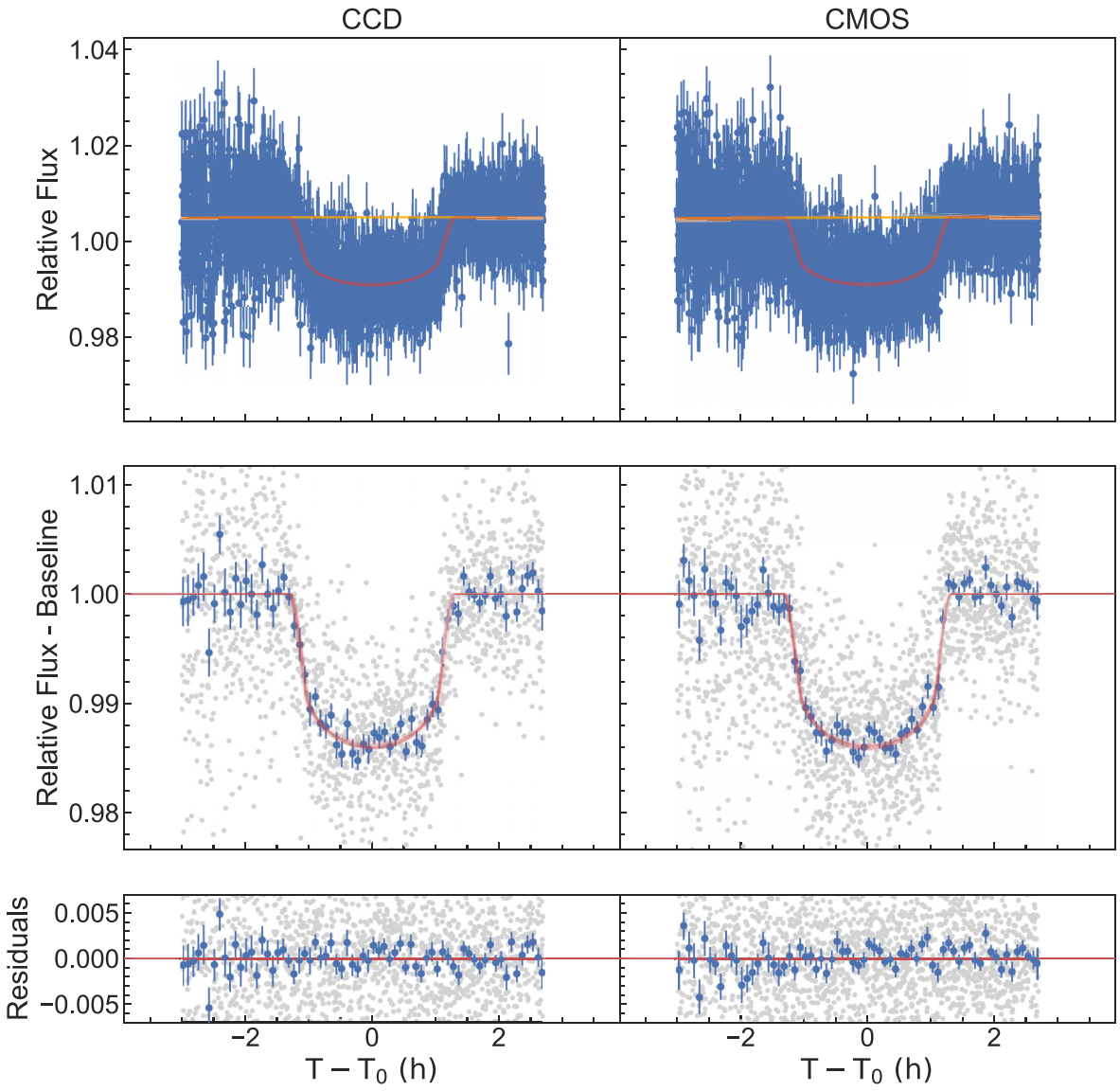


Figure A6. Same as in Fig. 7. Normalized light curves for the transiting system of WASP-97 (TIC 230982885) from NGTS on 2024 August 6.

Downloaded from academic.oup.com/rasti/article/doi/10.1093/rasti/rzag022/8530553 by claudia Legler user on 03 November 2026

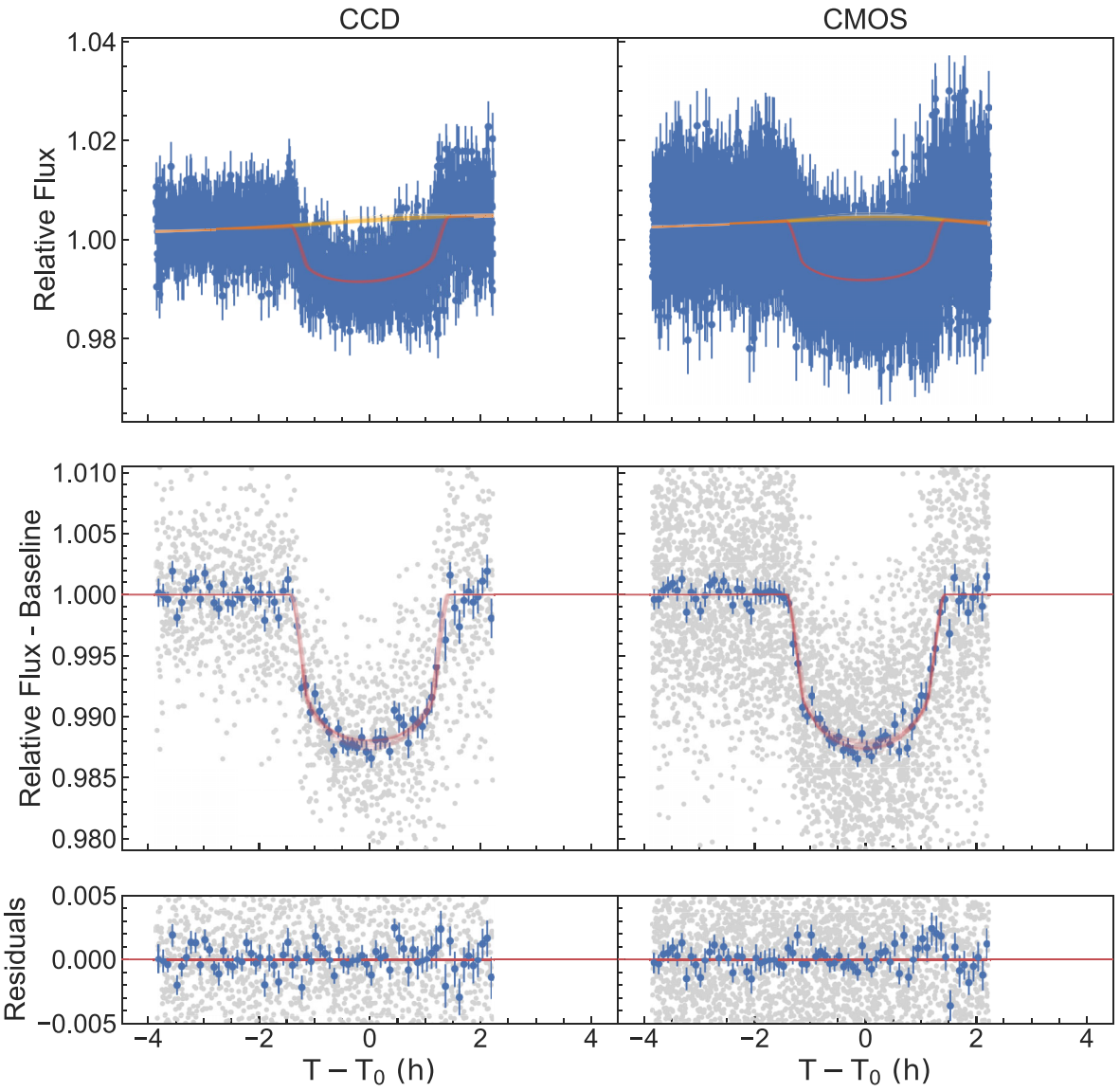


Figure A7. Same as in Fig. 7. Normalized light curves for the transiting system of WASP-95 (TIC 144065872) from NGTS on 2024 August 7.

Downloaded from academic.oup.com/rasti/article/doi/10.1093/rasti/rzag022/8530553 by claudia Legler user on 03 November 2026

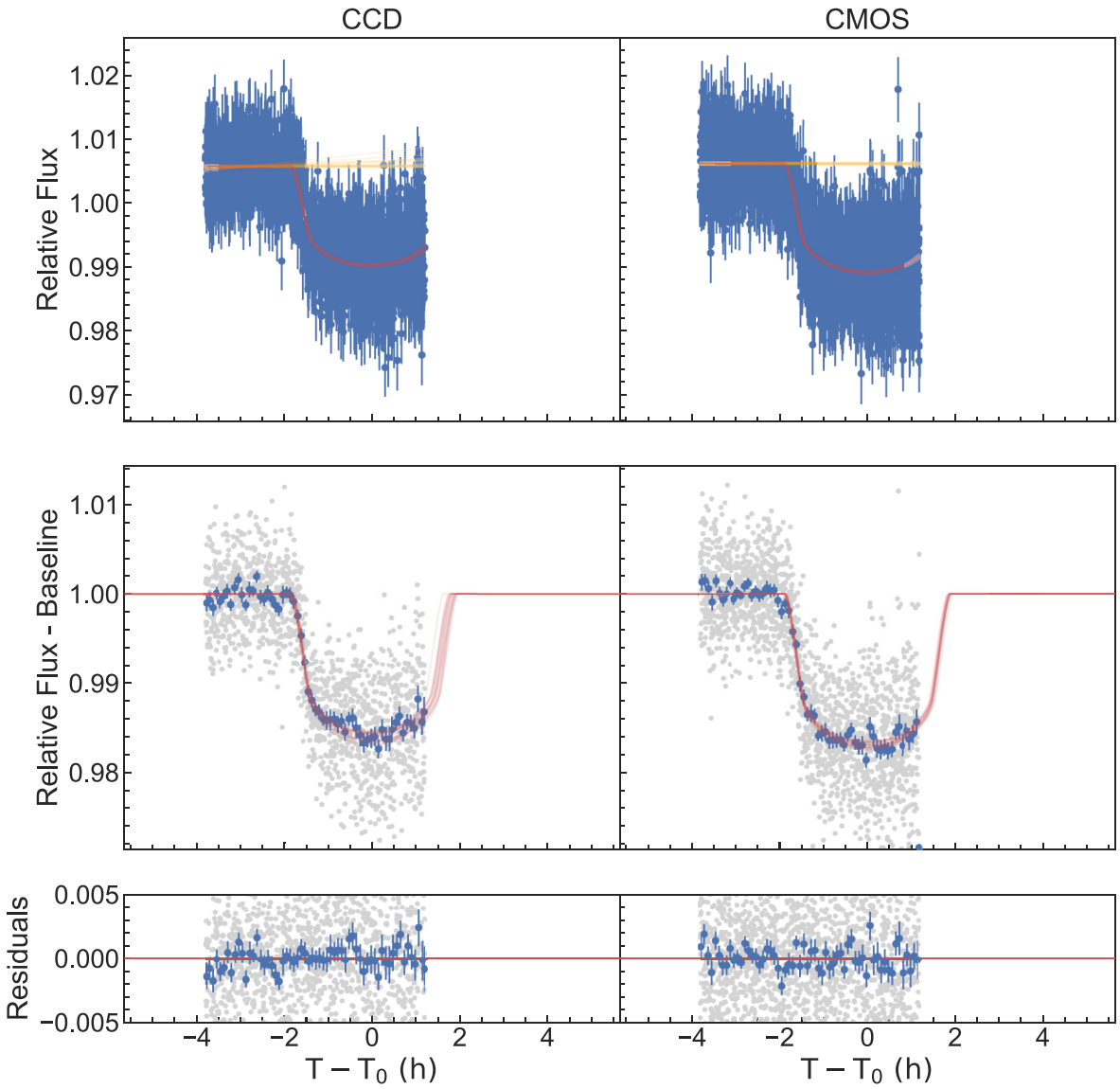


Figure A8. Same as in Fig. 7. Normalized light curves for the transiting system of KELT-10 (TIC 269217040) from NGTS on 2024 August 26.

Downloaded from academic.oup.com/rasti/article/doi/10.1093/rasti/rzag022/8530553 by claudia Legler user on 03 November 2026

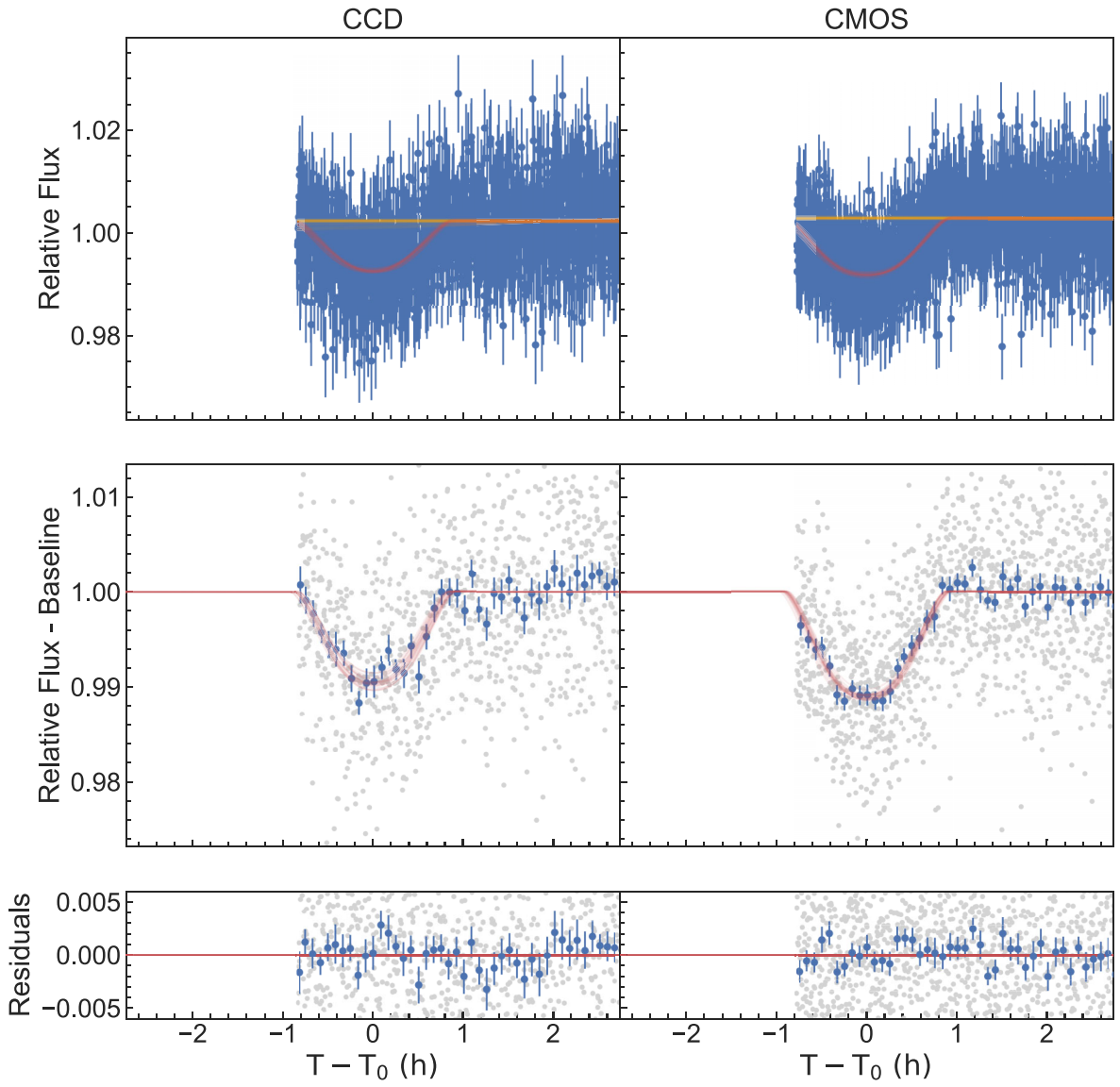


Figure A9. Same as in Fig. 7. Normalized light curves for the transiting system of TOI-4463 (TIC 8599009) from NGTS on 2024 August 27.

Downloaded from academic.oup.com/rasti/article/doi/10.1093/rasti/rzag022/8530553 by claudia Legler user on 03 November 2026

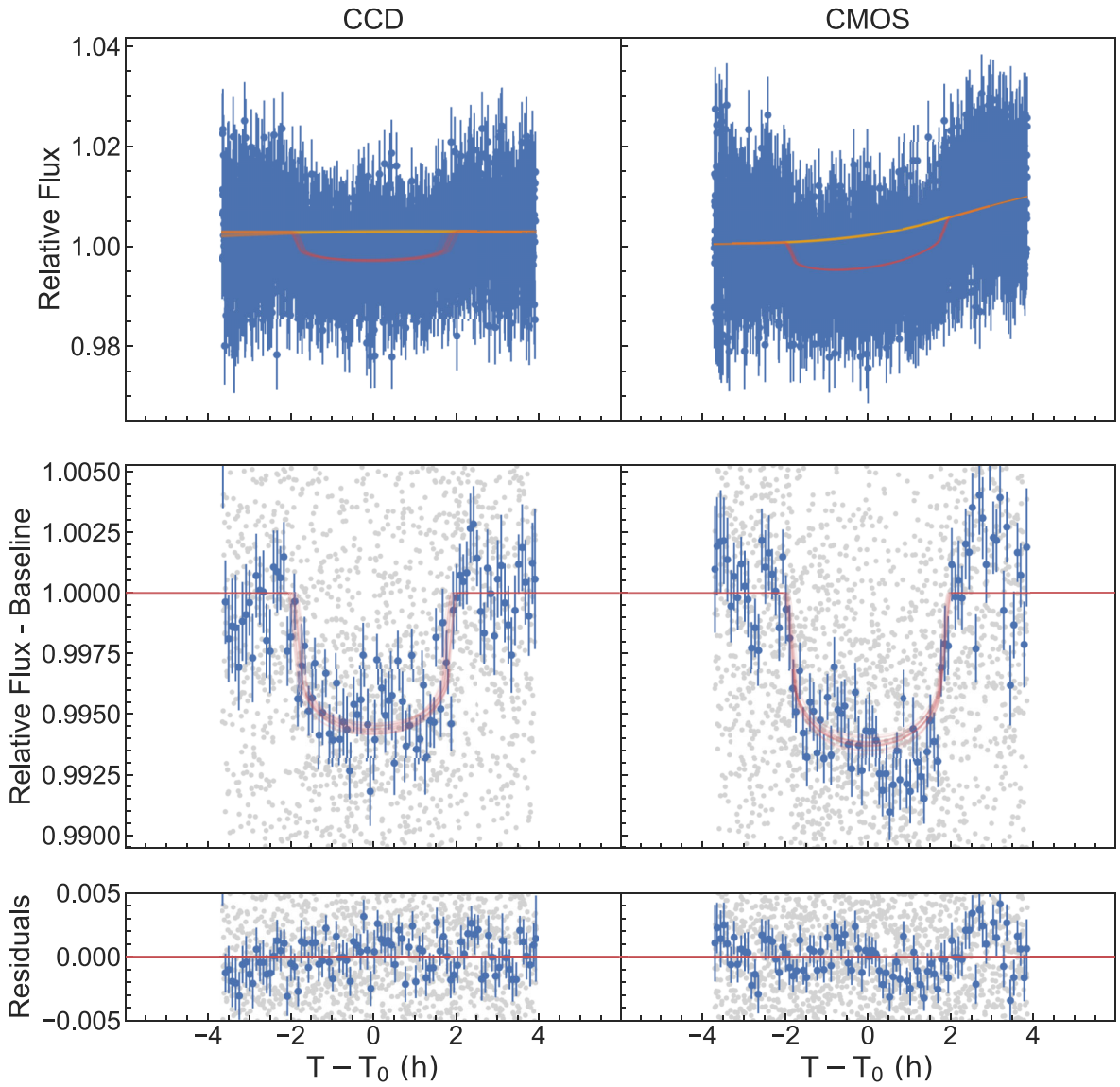


Figure A10. Same as in Fig. 7. Normalized light curves for the transiting system of WASP-30 (TIC 9725627) from NGTS on 2024 August 28.

This paper has been typeset from a TEX/LATEX file prepared by the author.

Downloaded from academic.oup.com/rasti/article/doi/10.1093/rasti/rzag022/8530553 by claudia Legler user on 03 November 2026

© The Author(s) 2026. Published by Oxford University Press on behalf of Royal Astronomical Society. This is an Open Access article distributed under the terms of the Creative Commons Attribution License (https://creativecommons.org/licenses/by/4.0/), which permits unrestricted reuse, distribution, and reproduction in any medium, provided the original work is properly cited.